The linked complexity of coseismic and postseismic faulting revealed by seismo-geodetic dynamic inversion of the 2004 Parkfield earthquake

Nico Schliwa [1], Alice-Agnes Gabriel [2,1], Jan Premus [3], František Gallovič [4]

[1]Ludwig-Maximilians-Universität München, Munich, Germany
[2]Scripps Institution of Oceanography, UC San Diego, La Jolla, CA, USA
[3]Côte d'Azur University, Nice, France
[4]Charles University, Prague, Czech Republic

This is a non-peer reviewed preprint submitted to EarthArXiv

Key Points:

- We perform a joint seismo-geodetic dynamic rupture and afterslip inversion of the 2004 Parkfield event.
- We find that coseismic rupture is separated into a strongly radiating pulse-like and a mildly radiating crack-like phase.
- Distinct dynamic rupture arrest mechanisms imprint on afterslip evolution and afterslip may drive delayed aftershocks.

Corresponding author: Nico Schliwa, `nico.schliwa@lmu.de`

Abstract

Several regularly recurring moderate-size earthquakes motivated dense instrumentation of the Parkfield section of the San Andreas fault, providing an invaluable near-fault observatory. We present a seismo-geodetic dynamic inversion of the 2004 Parkfield earthquake, which illuminates the interlinked complexity of faulting across time scales. Using fast-velocity-weakening rate-and-state friction, we jointly model 3D coseismic dynamic rupture and the 90-day evolution of postseismic slip. We utilize a parallel tempering Markov chain Monte Carlo approach to solve this non-linear high-dimensional inverse problem, constraining spatially varying prestress and fault friction parameters by 30 strong motion and 12 GPS stations. From visiting >2 million models, we discern complex coseismic rupture dynamics that transition from a strongly radiating pulse-like phase to a mildly radiating crack-like phase. Both coseismic phases are separated by a shallow strength barrier that nearly arrests rupture and leads to a gap in the afterslip. Coseismic rupture termination involves distinct arrest mechanisms that imprint on afterslip kinematics. A backward propagating afterslip front may drive delayed aftershock activity above the hypocenter. Analysis of the 10,500 best-fitting models uncovers local correlations between prestress levels and the reference friction coefficient, alongside an anticorrelation between prestress and rate-state parameters $b-a$. We find that a complex, fault-local interplay of dynamic parameters determines the nucleation, propagation, and arrest of both, co- and postseismic faulting. This study demonstrates the potential of inverse physics-based modeling to reveal novel insights and detailed characterizations of well-recorded earthquakes.

Plain Language Summary

The Parkfield section of the San Andreas plate boundary hosts regularly recurring moderate-size earthquakes. Seismic ground motions and slow deformation following the 2004 Parkfield earthquake were recorded by more than 30 seismometers and 13 GPS stations. While this is arguably one of the best-recorded earthquakes, it remains challenging to constrain the physics and properties at depth governing the earthquake from surface observations. Data-driven earthquake models solving inverse problems usually describe the kinematics of rupture. Here, we employ an expensive numerical algorithm to invert observations dynamically and find a physics-based set of parameters that simultaneously explain the earthquake and its afterslip, slow deformation following an earthquake. We find two separate phases of the earthquake that cause a similar amount of permanent displacement, but the rapid rupture of the first phase radiates much more potentially damaging seismic waves. The permanent displacement caused by the afterslip of the 2004 Parkfield earthquake exceeded its coseismic displacement. The local frictional properties that arrest the earthquake imprint on the subsequent afterslip evolution. Our approach illustrates that physics-based models utilizing modern computing techniques can reveal new insights and unprecedented detail even of well-studied events.

1 Introduction

The Parkfield section marks the transition between a locked part of the main strand of the San Andreas Fault (SAF) system and a creeping section to the northwest, with slip rates of 25–30 mm/yr (Titus et al., 2005; Tong et al., 2013). The transition between the creeping and locked sections is approximately at Middle Mountain (Murray & Langbein, 2006). Several earthquakes of $M_w \approx 6$ struck the Parkfield section in 1857, 1881, 1901, 1922, 1934, and 1966, corresponding to an average recurrence time of 22 ± 3 years (Bakun & McEvilly, 1984). The Parkfield earthquake prediction experiment (Bakun & Lindh, 1985) anticipated another $M_w \approx 6$ earthquake in 1988 ± 5 years and motivated dense seismic and geodetic instrumentation in the area. However, the anticipated Parkfield earthquake only happened in 2004 without noticeable short-term precursory signals (Bakun et al., 2005; Bilham, 2005). More than 40 strong-motion instruments and 13 GPS stations (Fig. 1) recorded the 2004 Parkfield earthquake and its afterslip with an epicentral distance of less than 32 km (e.g., Liu et al., 2006; Johnson et al., 2006).

1.1 Kinematic source inversion and back-projection imaging

Kinematic source inversions and back-projection studies of the 2004 Parkfield earthquake reveal a heterogeneous rupture process regarding slip, rupture speed, and rise time. The inferred kinematic models generally agree that the rupture process was complex despite its moderate size, with coseismic slip mainly confined within a depth of 4–10 km (e.g., Langbein et al., 2006). Most models suggest a primary high slip patch surrounding the hypocenter and a second major slip area, 15–20 km northwest of the hypocenter (Johanson et al., 2006; Liu et al., 2006; Custódio et al., 2009; Twardzik et al., 2012), with purely geodetic models being generally smoother (Kim & Dreger, 2008; Page et al., 2009). Some studies (Fletcher et al., 2006; Custódio et al., 2009) concluded that there

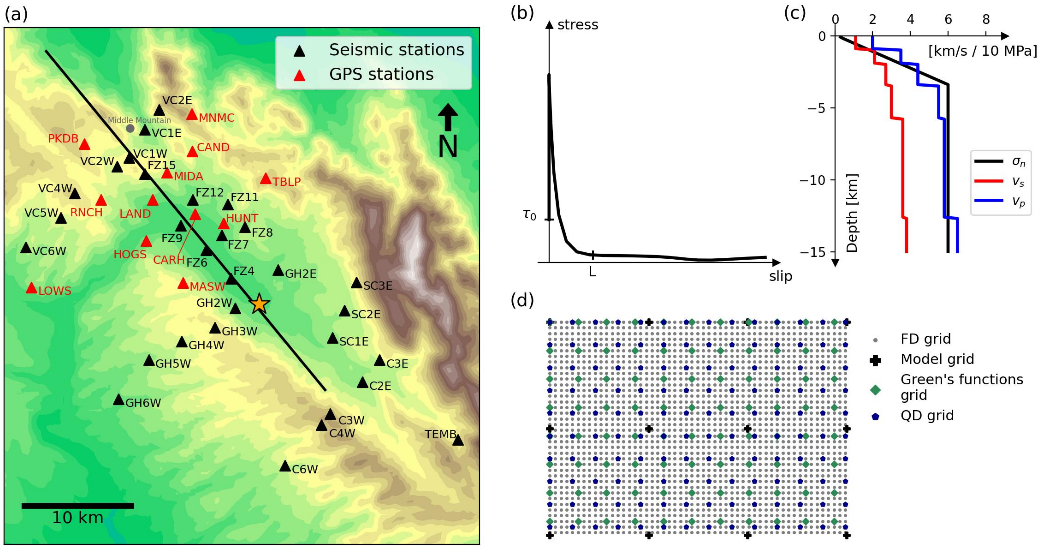

Figure 1. (a) Map view of the model domain with near-fault stations utilized in the dynamic inversion. Black triangles show seismic stations, red triangles are GPS stations, the black line is the fault trace, and the star marks the epicenter location. Topography is shown for regional context but is not accounted for in our forward models. (b) Exemplary stress evolution during coseismic dynamic rupture governed by the fast-velocity-weakening rate-and-state friction law measured in one of our dynamic rupture simulations. τ_0 represents the prestress and L the characteristic slip distance over which the frictional resistance drops from its static to its dynamic value. (c) Assumed depth-dependent normal stress σ_n and averaged seismic velocity profile used in the finite difference solver. We use two different seismic velocity profiles to compute different Green's functions for each side of the fault, respectively, following (Custódio et al., 2005). (d) Illustration of the four different grids discretizing the fault plane used in the dynamic source inversion. Dynamic model parameters are defined on the coarsest grid (model grid, black crosses) and bilinearly interpolated on the finest grid used in the finite-difference dynamic rupture solver (FD grid, grey dots) and the grid used in the quasi-dynamic boundary element method (QD grid, blue dots). Slip rates and slip from the FD or QD grids are averaged on the Green's functions grid (green dots) to compute synthetic seismograms and GPS displacements.

was rapid rupture onset with rupture velocities close to the S-wave speed ($\approx$ 3.6 km/s at hypocentral depth) and rise times shorter than 1 s. Propagating to the northwest, rupture speed may have decreased and rise times increased (Fletcher et al., 2006; Ma et al., 2008; Custódio et al., 2009).

Data-driven, kinematic earthquake models use various datasets to illuminate the space-time evolution of both coseismic rupture and afterslip. Still, they typically cannot probe dynamically consistent pre-, co-, and post-seismic mechanical conditions of faulting. Dynamic rupture forward modeling, on the other hand, is typically limited to the coseismic timescale and compares simulation results retrospectively to observational data or kinematic models (e.g., Ulrich et al., 2019; Tinti et al., 2021; Taufiqurrahman et al., 2023; Wen et al., 2024).

1.2 Results from previous dynamic modeling

Several studies investigated the dynamic source process of the 2004 Parkfield earthquake. Ma et al. (2008) constructed a dynamic rupture forward model using a linear slip-weakening friction law with mostly uniform frictional properties and a constant seismic S parameter (Andrews, 1976) for regions with a positive stress drop. S is the ratio of the strength excess over the expected stress drop, $S = \frac{\tau_y - \tau_0}{\tau_0 - \tau_d}$, where τ_y is the yield stress ($\sigma_n f_0$), τ_0 is the initial stress, and τ_d is the dynamic frictional stress ($\sigma_n f_w$). Their spatial distribution of the initial stress τ_0 is initially informed by a kinematic slip model (Custódio et al., 2005). They successively modify the initial stresses, τ_0, and choose the S parameter and the characteristic slip-weakening distance D_c by trial and error to match near-source ground motions.

Twardzik et al. (2014) performed a simple dynamic inversion to constrain the dynamic parameters that governed coseismic rupture. They assumed that the slip was confined to two elliptical patches and inverted for the geometry of the patches, the maximum S parameter within the patches, and the uniform background frictional properties of the fault plane. Barbot et al. (2012) created a long-term fully dynamic seismic cycle simulation of the Parkfield section, using a Dieterich-Ruina aging rate-and-state friction law (Ruina, 1983; Dieterich, 1992). They prescribed a heterogeneous spatial distribution of the difference between the friction parameters a and b, determining velocity-strengthening (VS) and velocity-weakening (VW) behavior. All other friction parameters were kept constant. Their model reproduced an earthquake sequence of irregular M_w 6.0 mainshocks with varying propagation directions. Kostka and Gallovič (2016) modified the dynamic model of Barbot et al. (2012) and showed that a stress perturbation, possibly caused by the nearby 1983 Coalinga-Nuñez earthquakes, may have delayed the occurrence of the 2004 Parkfield mainshock.

1.3 Afterslip and aftershocks

An extended period of exceptionally large postseismic deformation followed the 2004 Parkfield earthquake. At the surface, the San Andreas fault zone at Parkfield consists of two main fault branches, the main San Andreas fault (SAF) and the Southwest Fracture Zone (SWFZ), which are likely connected below 6 km depth (Simpson et al., 2006). During the 2004 Parkfield earthquake, the SWFZ ruptured coseismically. The SAF slipped postseismically, and afterslip at the surface was detected only hours after the event (Rymer et al., 2006; Langbein et al., 2006; Lienkaemper et al., 2006; Jiang et al., 2021a). Murray and Langbein (2006) estimated the moment of the postseismic slip during the first 60 days following the earthquake to be 2×10^{18} Nm, which is larger than the coseismic moment release of 1.3×10^{18} Nm. Postseismic slip occurred mainly above the coseismic rupture zone and further to the northwest (Langbein et al., 2006; Johanson et al., 2006). Surface afterslip reached 20–30 cm one year after the earthquake (Lienkaemper et al., 2006). Jiang et al. (2021a) combined high-rate with daily GPS solutions to study the early afterslip of the 2004 Parkfield event and found that early afterslip-associated stress changes appear synchronized with local aftershock rates.

Stress changes induced by coseismic slip and/or afterslip have been proposed to drive aftershock activity (e.g., Churchill et al., 2024). The 2004 Parkfield aftershocks appear mainly concentrated in two near horizontal streaks bordering the coseismic rupture zone, one between 4–6 km depth and the other one between 8–10 km depth (Thurber et al., 2006). Seismicity migrated along-strike and along-dip during the months after the earthquake, which has been interpreted as an indication of afterslip acting as the main driver of aftershocks (Peng & Zhao, 2009; Jiang et al., 2021a). However, Cattania et al. (2015) suggest that secondary triggering of aftershocks by earlier aftershocks may have played a more important role, and Churchill et al. (2022)'s global statistical analysis found no correlation between the relative afterslip moment and large aftershock activity.

1.4 Dynamic earthquake source inversion

The benefits of inverting for dynamic parameters to construct physically consistent source models have been recognized long ago (Fukuyama & Mikumo, 1993; Peyrat & Olsen, 2004; Twardzik et al., 2014), and recent advances in computational capabilities enable inverting for multiple spatial-variable dynamic parameters. Gallovič et al. (2019a) established a Bayesian dynamic source inversion framework, constraining the spatially variable linear slip-weakening friction dynamic parameters (fault prestress, strength and characteristic slip-weakening distance) across a finite, planar fault. This method has been applied to the 2016 M_w 6.2 Amatrice (Gallovič et al., 2019b) and 2020 M_w 6.8 Elazığ earthquake (Gallovič et al., 2020), using strong ground motion observations to constrain dynamic rupture parameters and quantify their uncertainties. Premus et al. (2022) extended the method to rate-and-state friction, which enables jointly simulating coseismic slip and afterslip in the same framework. Their dynamic source inversion of the 2014 M_w 6.0 South Napa California earthquake constrained by co- and postseismic strong ground motion and GPS data illuminated how variable prestress and frictional conditions on the fault govern the spatial separation between shallow coseismic and postseismic slip, the progression of afterslip driving deep off-fault aftershocks, and the coseismic slip distribution.

Here, we apply the approach introduced in Premus et al. (2022) to the extensive seismic and geodetic observations of the 2004 Parkfield earthquake. We are especially interested in investigating the interrelation of coseismic slip and the exceptionally large amount of afterslip in a uniform, data-driven modeling framework. We jointly invert this data to establish an ensemble of dynamic models that simultaneously describe the coseismic and three months of postseismic slip evolution. We detail the complex coseismic and postseismic faulting dynamics of a preferred joint model. We find new evidence for the coseismic rupture phase involving distinctly different rupture styles and explore the complex fault slip transition from the coseismic to the postseismic phase. We investigate which dynamic parameters govern different coseismic and afterslip rupture styles and analyze trade-offs between the dynamic parameters. We find different coseismic rupture termination mechanisms imprinting on the evolution of afterslip. We jointly quantify the average values and variability of coseismic source characteristics, including stress drop, fracture energy, and radiation efficiency, as well as afterslip kinematics such as rise time, propagation speed, and spatial heterogeneity and extent based on physics-based *and* data-driven models.

2 Methods

This section summarizes the forward and inverse modeling methods and seismic and geodetic data sets used in this study. First, we introduce the friction law that facilitates the dynamic description of our problem. Then, we present the two stages of our forward model and the respective numerical solvers. Next, we describe the Bayesian inversion method, the Parallel Tempering Markov chain Monte Carlo approach. We detail the data used to constrain the inversion and our model parameterization. Lastly, we present our inversion strategy.

2.1 Fast-velocity-weakening rate-and-state friction

We use a fast-velocity-weakening rate-and-state friction law (Ampuero & Ben-Zion, 2008; Noda et al., 2009) to simulate coseismic and postseismic slip in the same modeling framework (Premus et al., 2022).

The following equations govern the fault's frictional resistance (Fig. 1b, Dunham et al., 2011):

$$\tau = \sigma_n a \,\mathrm{arsinh}\left[\frac{\dot{s}}{2\dot{s}_0}\exp\left(\frac{\Psi}{a}\right)\right], \tag{1}$$

$$\frac{\mathrm{d}\Psi}{\mathrm{d}t} = -\frac{\dot{s}}{L}\Big(\Psi - \Psi_{SS}\Big), \tag{2}$$

$$\Psi_{SS} = a\log\left[\frac{2\dot{s}_0}{\dot{s}}\sinh\left(\frac{f_{SS}}{a}\right)\right], \tag{3}$$

$$f_{SS} = f_w + \frac{f_{LV} - f_w}{\Big(1 + \big(\frac{\dot{s}}{\dot{s}_w}\big)^8\Big)^{\frac{1}{8}}}, \tag{4}$$

$$f_{LV} = f_0 - \big(b - a\big)\log\left(\frac{\dot{s}}{\dot{s}_0}\right). \tag{5}$$

Eq. 1 gives the frictional resistance τ, which depends on the normal stress σ_n, the direct effect parameter a, the slip rate $\dot{s}$, the reference slip rate $\dot{s}_0$, and the state variable Ψ. Eq. 1 is regularized to avoid divergence at $\dot{s} = 0$ (Rice & Ben-Zion, 1996; Lapusta et al., 2000). Eq. 2 is an ordinary differential equation describing the evolution of the state variable Ψ. L is the characteristic slip distance, and Ψ_{SS} is the steady-state value of the state variable, which is given by Eq. 3. Eq. 4 computes the steady-state friction f_{SS}, which depends on the weakened friction coefficient f_w, the slip rate $\dot{s}$, the weakening slip rate $\dot{s}_w$, and the low-velocity steady-state friction coefficient f_{LV}. At $\dot{s} > \dot{s}_w$, f_{SS} drops rapidly from f_{LV} to f_w, with the $1/\dot{s}$ behavior resembling thermal weakening processes at coseismic slip rates such as flash-heating (Rice, 2006; Beeler et al., 2008). Eq. 5 calculates the low-velocity steady-state friction f_{LV} from the steady-state friction coefficient, the slip rate $\dot{s}$ and the reference slip rate $\dot{s}_0$, and the difference between the state evolution parameter b and the direct effect parameter a, which determines if the frictional behavior is velocity-weakening ($b-a > 0$) or velocity-strengthening ($b-a < 0$). We set the reference slip rate to 10^{-6} m/s, a common choice in dynamic rupture simulations (Harris et al., 2018). We note that the initial slip rate $\dot{s}_{init}$ is a dynamic inversion parameter (Table 1) and differs from the reference slip rate $\dot{s}_0$.

2.2 Joint dynamic rupture and afterslip forward model

The forward model consists of two stages, the coseismic and the postseismic phase, implemented using a 3D fully dynamic and a 3D quasi-dynamic method, respectively (Premus et al., 2022). In the coseismic stage, we model the earthquake dynamic rupture propagation with the code FD3D_TSN (Premus et al., 2020) based on an efficient GPU implementation of a finite-difference method. The code uses a fourth-order accurate staggered-grid method with a traction-at-split node implementation (Dalguer & Day, 2007) of the frictional fault interface condition.

The postseismic phase is modeled with a 3D quasi-dynamic boundary element approach (Rice, 1993; Gallovič, 2008). We solve the quasi-dynamic problem with a fifth-order Runge-Kutta method with adaptive time stepping. Both stages share the same planar fault geometry and the same distribution of dynamic parameters but will be constrained by complementary observations. The final coseismic distributions of the shear stress, slip rate, and state variable are used as the initial values of the postseismic stage.

Synthetic seismograms and static displacements are calculated via precomputed Green's functions (Okada, 1985; Cotton & Coutant, 1997).

3D dynamic rupture simulations are computationally expensive, and using rate-and-state friction laws increases this cost compared to linear-slip weakening friction (e.g., Heinecke et al., 2014; Uphoff et al., 2017; Krenz et al., 2021). Monte-Carlo-based Bayesian inversion approaches require many forward models (e.g., Press, 1968). Therefore, our joint dynamic coseismic and afterslip inversion requires large computational resources. The coseismic dynamic rupture propagation stage spans the first 21 s of the forward model, after which slip rates are low enough ($< 10^{-2}$ m/s) to switch to the quasi-dynamic simulation in the postseismic stage lasting for 90 days. We use a finite-difference grid spacing of 100 m (Fig. 1d), which sufficiently samples the critical length scale of dynamic rupture, the process zone at the rupture tip, with an average of 6.3 points, ensuring accuracy (Day et al., 2005). The grid spacing of the quasi-dynamic solver is 400 m.

2.3 Bayesian inversion method

We use a Bayesian framework to formulate the inverse problem (Tarantola, 2005; Gallovič et al., 2019a), where we sample the posterior probability density function (PDF) $p(\mathbf{m}|\mathbf{d})$ to gain information on the likelihood of a set of dynamic model parameters $\mathbf{m}$ given the observed seismic waveform and geodetic displacement data $\mathbf{d}$:

$$p(\mathbf{m}|\mathbf{d}) = \frac{p(\mathbf{m})p(\mathbf{d}|\mathbf{m})}{p(\mathbf{d})}. \tag{6}$$

We prescribe the prior PDF $p(\mathbf{m})$ as a uniform distribution between the pre-selected dynamic parameter bounds (see Table 1). The Bayesian evidence $p(\mathbf{d})$ normalizes the posterior PDF. The PDF of the data given a model $p(\mathbf{d}|\mathbf{m})$ is based on a least-square misfit between the synthetics $\mathbf{s}_i(\mathbf{m})$ and the observed data $\mathbf{d}_i$:

$$p(\mathbf{d}|\mathbf{m}) = \exp\bigg(-\frac{1}{2}\sum_{i=1}^{N} \frac{||\mathbf{s}_i(\mathbf{m}) - \mathbf{d}_i||^2}{\sigma_i^2}\bigg). \tag{7}$$

N is the total number of stations, and σ_i are the standard deviations, which are assumed to be uncorrelated and represent the combined uncertainty of the model and data errors.

We explore the model space with the Parallel Tempering Markov chain Monte Carlo (MCMC) method (Sambridge, 2013). A Markov chain consists of a sequence of models where the parameters of the next model depend only on the previous model. Model parameters are randomly perturbed during each step, with the step size inferred from a log-normal distribution. The new model is checked against the parameter bounds and is either directly discarded if the bounds are violated or the algorithm runs the forward simulation and calculates the misfit. Proposed models with a smaller misfit are always accepted. If the new misfit is larger, the proposed model is accepted with a probability given by the Metropolis-Hastings rule (Metropolis et al., 1953). The Parallel Tempering approach explores the model space using several parallel Markov Chains, each with a temperature parameter T assigned. These Markov chains sample a modified posterior PDF:

$$p(\mathbf{m}|\mathbf{d}, T) = c_1 p(\mathbf{m}) \exp\left(- \frac{1}{T} \frac{1}{2} \sum_{i=1}^{N} \frac{||\mathbf{s}_i(\mathbf{m}) - \mathbf{d}_i||^2}{\sigma_i^2} \right). \tag{8}$$

Markov Chains with higher T have smoother PDFs, which increases the probability of accepting the next step and facilitates the escape from local minima. c_1 normalizes the PDF.

The Parallel Tempering algorithm proposes a temperature swap between the chains after each iteration. The probability of each swap is based on the Metropolis-Hastings rule. Final samples of the posterior PDF are drawn from the chains where $T = 1$. Sambridge (2013) demonstrated that the Parallel Tempering method is well-suited for non-linear problems with complicated PDFs and may converge more than 10 times faster than a non-tempered MCMC approach. In our specific case, each MPI rank hosts 8 Markov Chains, two with $T = 1$, and the other six temperatures are randomly drawn from a log-uniform distribution between 1 and 100, concentrating more values close to 1.

2.4 Seismic and geodetic data

We include seismic and geodetic measurements, both on coseismic and postseismic time scales, as inversion data. To constrain the coseismic rupture dynamics, we use strong-motion observations at 30 near-fault stations (Fig. 1a). We excluded several near-fault stations due to missing origin times, strong fault zone effects apparent even at low frequencies, or pronounced site amplifications (Liu et al., 2006). We include only horizontal components due to the worse signal-to-noise ratio of vertical components and because

Table 1. Minimum and maximum values of the dynamic parameters subject to the inversion. $\dot{s}_w$ and $\dot{s}_{init}$ can only vary in the velocity-strengthening areas of the fault and have constant values of 0.1 m/s and 10^{-12} m/s in the velocity-weakening areas, respectively.

Label	Parameters	Minimum Value	Maximum Value
τ_0	Shear prestress	10^3 Pa	2×10^9 Pa
$b - a$	Difference between the direct effect and the state evolution parameter	-0.03	0.03
f_0	Reference friction coefficient at $\dot{s}_0 = 10^{-6}$	0.2	1.5
L	Characteristic slip distance	0.004 m	1.0 m
$\dot{s}_w$	Weakening slip rate	0.01 m/s	2.0 m/s
$\dot{s}_{init}$	Initial slip rate	10^{-13} m/s	1.21×10^{-9} m/s
h_x	Along-strike position of nucleation patch	28.0 km	32.0 km
h_z	Along-dip position of nucleation patch	6.5 km	9.0 km
r_{nuc}	Radius of the nucleation patch	225 m	450 m
σ_{nuc}	Stress increase within the nucleation patch	1%	60%

we do not allow for dip-slip (see Sec. 2.5). De-emphasizing vertical components is a common assumption, e.g., Liu et al. (2006) down-weight the vertical components by a factor of 10. The strong-motion data is integrated to velocities and filtered by a fourth-order causal Butterworth filter between 0.16 Hz and 0.5 Hz. We choose a low-frequency limit of 0.16 Hz to ensure a flat frequency response of all instruments (Custódio et al., 2005). The chosen upper limit of 0.5 Hz mitigates the impact of the 3D velocity structure, in particular, of the low-velocity fault zone, which may affect all near-fault stations (Li et al., 1990; Lewis & Ben-Zion, 2010). We use 25 s long seismic waveforms during the convergence phase (see Sec. 2.6). In the subsequent sampling phase, we limited the coseismic waveforms to 15 s long waveforms. The chosen relatively short time windows of 25 s or 15 s reduce contamination from seismic reverberations due to the 3D subsurface structure. We assume a universal data uncertainty of $\sigma = 0.05$ m/s when computing the posterior probability density function (PDF) of the data (Eq. 7).

We use the preprocessed horizontal GPS data by Jiang et al. (2021a) that span both coseismic and postseismic periods. Namely, we include the coseismic displacements at

12 GPS stations (Fig. 1a) and postseismic displacements at 11 GPS stations during the 90-day postseismic period. We compare the postseismic observations with our synthetics at 35 logarithmically-spaced points in time to increase the weight and resolution of the early afterslip phase. We excluded the postseismic data from the GPS station CARH as it is located between the main trace of the SAF and the secondary SWFZ branch southwest of the SAF. Afterslip migrating from the SWFZ to the SAF likely led to the polarity change of the postseismic deformation measured at CARH (Murray & Langbein, 2006; Jiang et al., 2021a), an effect which our single fault model cannot capture. We completely exclude the GPS station POMM from our analysis since it is located directly above the SWFZ and is likely strongly affected by small-scale complexities in fault geometry that we cannot capture in our planar fault model (Murray & Langbein, 2006; Custódio et al., 2009). We assign an individual uncertainty value to each GPS station calculated from the mean of the data uncertainty as given by Jiang et al. (2021a) during the included 90-day period.

2.5 Model setup

Our dynamic rupture and afterslip forward model incorporates a single planar fault with a strike of 320.5° and dip of 87.2° based on the fault geometry of the SWFZ of Jiang et al. (2021a). The Green's functions account for the fault dip, but the dynamic rupture and quasi-dynamic models assume a vertical fault plane similar to (Gallovič et al., 2019a, 2019b; Premus et al., 2022). We place the hypocenter in the initial dynamic rupture model at 35.8154°N, 120.3667°W, and 7.5 km depth based on a matched filter relocated earthquake catalog (Neves et al., 2022). We use two different 1D velocity profiles (Custódio et al., 2005) to calculate Green's functions accounting for different materials on each side of the fault (Table S1). The coseismic model assumes an average of both 1D layered velocity profiles, while the postseismic model assumes a homogenous medium, with $v_s =$ 3600 m/s, $v_p = 5800$ m/s, and $\rho = 2700$ kg/m^3. The coseismically used Green's functions account for viscoelastic attenuation. We assume variable Q values based on the empirical relationship v_s: $Q_s = 0.1\, v_s$ (in m/s) and $Q_p = 1.5\, Q_s$ (Olsen et al., 2003).

Table 1 summarizes the six dynamic parameters ($\tau_0, b{-}a, f_0, L, \dot{s}_w, \dot{s}_{init}$) and four coseismic rupture nucleation parameters (h_x, h_z, r_{nuc}, σ_{nuc}) subject to Bayesian inversion. We fix the weakened friction coefficient f_w to a constant value of f_w=0.3 following Ma et al. (2008) and vary only the reference friction coefficient f_0, and, thereby, the "reference friction drop", $f_0 - f_w$. Similarly, we fix the direct effect parameter a to a constant value of a =0.015 and allow b to vary, altering the difference $b-a$. We assume pure strike-slip faulting without dip-slip components in both the modeling and inversion stages. Thus, the prestress τ_0 and s_{init} are scalars. The dynamic parameters (prestress and friction parameters) are defined on the model grid with 24 points along-strike and 9 points along-dip (Fig. 1d). In between the grid points, the dynamic parameters are bilinearly interpolated on the denser FD (finite-difference) and QD (quasi-dynamic) grids. The such defined number of potentially free dynamic inversion parameters is 1300. However, $\dot{s}_w$ and $\dot{s}_{init}$ can only vary in the velocity-strengthening areas of the fault and have constant values of 0.1 m/s and 10^{-12} m/s in the velocity-weakening areas, respectively. The constant $\dot{s}_w$ and $\dot{s}_{init}$ in the velocity-weakening regions simulate locked asperities. Therefore, the number of effectively free parameters is approximately 1100 and can dynamically change throughout the inversion.

We use a temporary (for 1 s) overstressed nucleation patch around the hypocenter to initiate dynamic rupture. We invert for the radius of this nucleation patch and the associated shear stress increase. The along-strike and along-dip location of the center of the nucleation patch, the hypocenter, is also subject to the inversion (see Table 1).

The effective normal stress linearly increases until a depth of 3.5 km (Fig. 1c) and then remains constant at 60 MPa at deeper depths (Rice, 1992; Suppe, 2014; Madden et al., 2022). Our profile is similar to the normal stress profile in a previous 2004 Parkfield dynamic rupture forward model (Ma et al., 2008).

2.6 Inversion strategy

Dynamic source inversion is challenging due to the nonlinear, ill-posed nature of the very high-dimensional problem and the complicated non-convex shape of the misfit function. We aim to increase the inversion's performance by choosing an initial model (IM) with a high probability density (close to the optimal model). We split the dynamic inversion workflow into a convergence phase and a sampling phase. The latter generates the ensemble for uncertainty quantification. During the convergence phase, we manually modify model parameters, adjust weights and datasets, and restart the Markov chains to achieve faster convergence. Thus, only the sampling phase represents an undisturbed

MCMC inversion. The maximum likelihood model of the convergence phase serves as the starting model of the sampling phase. Only a few Markov chain links separate this starting model from our preferred model (Sec. 3.2)

A randomly chosen IM may not nucleate self-sustained rupture or produce a much larger moment magnitude than the target earthquake. Therefore, we construct an initial dynamic rupture model based on the stress drop and final slip distribution of "Model B" of Ma et al. (2008), who use linear slip-weakening friction to model the coseismic rupture of the 2004 Parkfield earthquake. We choose the potential stress drop ($\tau_0 - \tau_d$) distribution of our IM to resemble the final slip distribution of Ma et al. (2008). Then, we adapt our S parameter and weakening distance L to approximately reproduce their rupture velocity distribution using a few trial-and-error simulations. In addition, we randomly perturb the characteristic slip distance L and the prestress τ_0 by up to $\pm 10\%$ to include small-scale heterogeneity and rupture complexity. We note that our resulting dynamic parameters (see Fig. S1) deviate from Ma et al. (2008), e.g., due to the different friction laws used.

Albeit the random perturbations, the rupture of the IM is very homogeneous (Fig. S2). The IM's fit to the data is moderate (see Figs. S3 and S4). It yields a seismic variance reduction of 0.04 and a coseismic GPS variance reduction of 0.87.

The first $\approx 500,000$ models generated during the convergence phase focus on the coseismic dynamic rupture phase (21 seconds) and 69 seconds of early afterslip. Then, we modify the best-fit model from this convergence ensemble to capture long-term (90-day) afterslip observations. We manually increase the initial slip rate and potential stress drop in certain velocity-strengthening areas to approximately match the afterslip distribution of Jiang et al. (2021a) and the GPS-only model of Johanson et al. (2006). To suppress anomalously high afterslip at the free surface, we set the reference friction coefficient to 1.2 and the prestress below 1 MPa at the free surface's model grid points.

The convergence phase, including long-term afterslip, additionally visits $\approx 700,000$ models. During the convergence phase, we adjust the weighting of the different data sets (strong-motion, coseismic GPS, and postseismic GPS) to ensure their respective misfits remain of the same order of magnitude. Similarly, we successively reduce the step size of the inversion parameter perturbations to keep the model acceptance rate above 10% (Table S2). We restart the Markov chains several times after finding a model with a significantly improved misfit. This model then serves as a new starting model for all otherwise independent MPI ranks of the inversion algorithm (see Sec. 2.3).

We start the sampling phase after reaching a satisfying data misfit. In this final phase representing a true MCMC inversion, we let the chains sample the model space without manual interventions to obtain an ensemble of best-fitting models that can explain the data similarly well. The final sampling phase of the inversion visits $\approx 800,000$ models. The resulting best-fitting model ensemble contains 10,500 unique models. During the sampling phase, all inversion meta-parameters are kept constant.

We run the inversion on a server with 8 Nvidia RTX A5000-GPUs and 32 AMD-EPYC-7313 CPU cores with a 3 GHz base frequency. We compute the coseismic stage on the GPUs and the postseismic stage on the CPUs. This hybrid approach allows us to exploit the hardware architecture efficiently using 24 MPI ranks (3 ranks per GPU). One solution of the joint forward model takes, on average, 5 minutes. Therefore, we can visit, on average, 4.8 joint forward models per minute. Overall, the inversion visited more than 2 million joint simulations. This sums up to over 300 days of runtime on our server or >57,000 hours on a single GPU.

3 Results

3.1 Initial dynamic rupture model

Our initial dynamic rupture model (IM), which is extended from the dynamic rupture model by Ma et al. (2008), already reveals interesting dynamic aspects of the 2004 Parkfield rupture. We find that an unusually low potential stress drop and reference friction drop ($f_0 - f_w$) are needed to match the large-scale rupture characteristics of the 2004 Parkfield earthquake. The earthquake ruptured over an area larger than 20 km along strike while coseismic slip remained mostly below 25 cm, which is small considering its magnitude of M_w 6.0 (Brengman et al., 2019) and in agreement with previous observational studies (e.g., Liu et al., 2006; Custódio et al., 2009). The IM requires a low average potential stress drop to facilitate dynamic rupture across a wide area with a small average slip. In the IM, we set the potential stress drop to 3.0 MPa within the hypocentral area and to only 0.6 MPa elsewhere, where we expect coseismic rupture (see Fig. S5). Outside of the expected rupture area, the potential stress drop gradually decreases to −3.0 MPa.

A lower stress drop generally reduces rupture velocity (Andrews, 1976; Gabriel et al., 2012). However, several studies observed that the average rupture velocity of the 2004 Parkfield earthquake is relatively fast at 2.5–3.5 km/s (e.g., Fletcher et al., 2006; Ma et al., 2008; Custódio et al., 2009). To achieve a dynamic rupture model that combines a low stress drop with moderate-to-high rupture velocity, we set the characteristic slip distance within the coseismic rupture area to a small value of $L = 2$ cm and assume a small S parameter, the ratio of the strength excess over the expected stress drop. Since the weakened friction coefficient ($f_w = 0.3$) and the potential stress drop are prescribed in the IM, we choose a small reference friction $f_0 = 0.313$. This leads to a reference friction drop of only 0.013, which is unusually low compared to common dynamic rupture simulation parameterizations (e.g., 0.4 in Harris et al., 2018). However, such a small reference friction value is in line with results obtained from dynamic modeling of afterslip following the 2004 Parkfield earthquake (Chang et al., 2013).

3.2 Preferred joint dynamic rupture and afterslip model

Next, we present our preferred joint dynamic rupture and afterslip model (PM) in terms of coseismic and postseismic rupture characteristics, fit to the seismic and geodetic observations, and distribution of dynamic parameters. We chose the PM, which is a joint dynamic rupture and 90-day afterslip simulation, to maximize the sum of the seismic and combined (coseismic + postseismic) GPS data variance reductions (VR). The PM model selected by this criterion achieves a better seismic fit compared to the maximum likelihood model of the inversion.

3.2.1 Dynamic parameters of the preferred joint dynamic rupture and afterslip model

Fig. 2 shows the six dynamic parameters of our PM, which are subject to the Bayesian inversion. We do not show parameters on those parts of the faults that we consider unconstrained by the inversion due to the fact that the sum of the co- and postseismic slip amplitudes remains too small.

3.2.1.1 Potential stress drop, velocity-weakening and velocity-strengthening friction

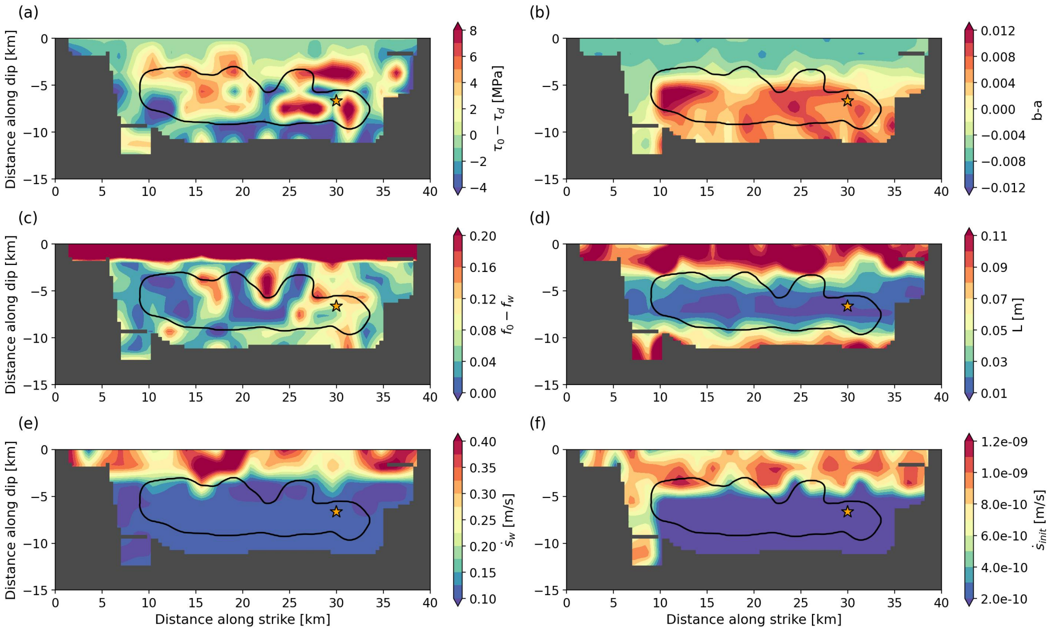

Figure 2. Dynamic parameters of the preferred joint dynamic rupture and afterslip model (PM) resulting from the Bayesian inversion. The parameters are bilinearly interpolated from the model grid (Fig. 1d) onto the grid of the quasi-dynamic solver, which has a 400 m spacing. We consider parameters to be unconstrained in all areas of the fault where the overall fault slip (coseismic + postseismic) does not exceed 10 cm within a radius of 1.2 km. We do not show dynamic parameters on these unconstrained fault grid points. The black line indicates the extent of the coseismic rupture, and the star marks the hypocenter of the mainshock. (a) Potential stress drop $\tau_0 - \tau_d$. (b) Difference between the state evolution and the direct effect parameter, $b - a$. (c) Reference friction drop $f_0 - f_w$. (d) Characteristic slip distance L. (e) Weakening slip rate $\dot{s}_w$. (f) Initial slip rate $\dot{s}_{init}$.

We analyze the potential stress drop, defined as $\tau_0 - \tau_d$, with the absolute prestress τ_0 and $\tau_d = f_w \sigma_n$. The spatial average of the potential stress drop within the coseismic rupture area is 1.0 MPa with a standard deviation of 3.4 MPa. We define the coseismic rupture area as the region where coseismic slip exceeds 0.01 m, and the fault slip area as the region where the overall slip (coseismic + postseismic) exceeds 0.1 m within a radius of 1.2 km (visible area in Fig. 2). The fault slip area also includes well-constrained strength barriers. When considering the fault slip area, the spatial average potential stress drop reduces to 0.5 MPa, and the standard deviation to 3.0 MPa.

Within the coseismic rupture area, $b-a$ remains dominantly positive, which is associated with VW behavior. The spatial average value is 0.0037, and the standard deviation is 0.0048. The standard deviation being larger than its average is associated with the dynamic rupture penetrating the shallowest portion of the fault where $b-a$ is negative. For the fault slip area, including regions hosting afterslip, the spatial average of $b-a$ drops to 0.000 with a standard deviation of 0.0059. The respective $b-a$ averages in the VS and VW regions are comparable to the non-constant values of Barbot et al. (2012)'s dynamic seismic cycling model, which can be approximated by $b - a = 0.004$ within the coseismic rupture area and $b-a = -0.004$ within the VS regions. The range of $b-a$ within the shallow VS region agrees with the values obtained from a dynamic afterslip inversion (Chang et al., 2013).

3.2.1.2 Reference friction drop and characteristic slip distance

The spatial average reference friction drop within the coseismic rupture area is 0.058, and its standard deviation is 0.049. The average coseismic reference friction drop clearly increases compared to the IM (0.013) but is still small. Parts of the fault exhibit a negative reference friction drop. The average reference friction drop increases considerably to 0.164 when including the afterslip regions. However, this value is strongly affected by the high reference friction coefficients at the free surface.

The average characteristic slip distance L within the coseismic rupture area is 0.030 m with a standard deviation of 0.024 m, corresponding to a coefficient of variation (CV; the ratio of standard deviation to average value) of CV = 0.80. The average and the standard deviation increase to values of 0.057 m and 0.045 m, respectively, when including the afterslip regions. L noticeably increases above and beneath the top and bottom rupture edges, respectively.

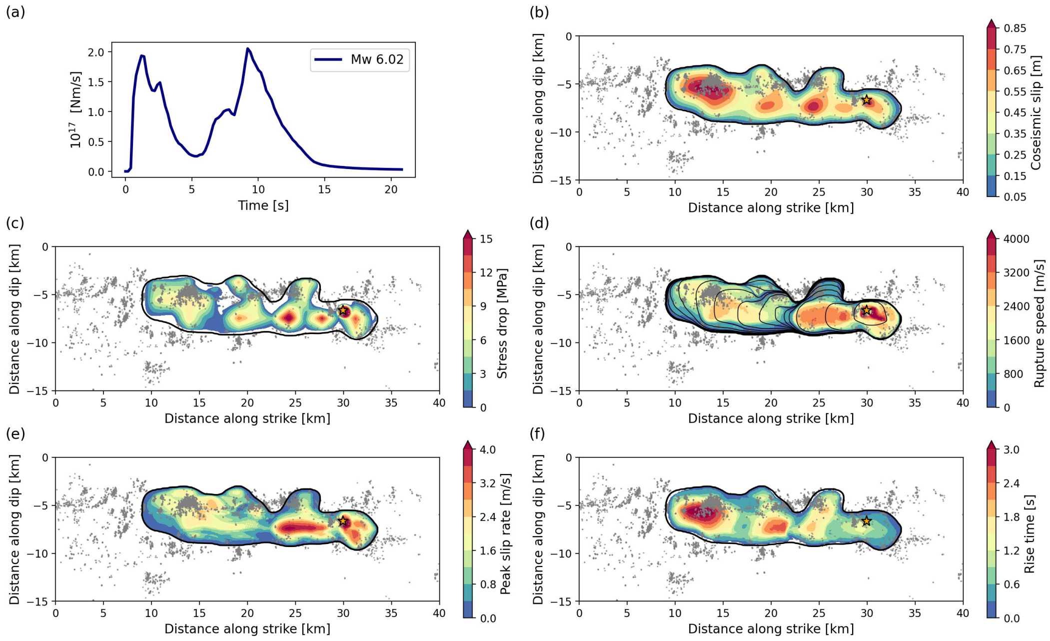

Figure 3. Coseismic dynamic rupture parameters of the PM. Grey dots show 90-day aftershock locations (Neves et al., 2022) projected on the planar fault plane, the black contour indicates the coseismic rupture extent, and the star marks the hypocenter. (a) Moment release rate and moment magnitude. (b) Coseismic slip. (c) Stress drop. (d) Local rupture speed and rupture front contours every 1 s. (e) Peak slip rate. (f) Rise time.

3.2.1.3 Weakening and initial slip rates

The weakening slip rate $\dot{s}_w$ and the initial slip rate $\dot{s}_{init}$ are allowed to vary only within VS regions (Sec. 2.5). The $\dot{s}_{init}$ distribution shows that the shallow afterslip regions mostly creep at a slip rate of 10^{-9} m/s, which is close to the plate rate. In the shallow afterslip regions, $\dot{s}_w$ increases to values larger than 0.2 m/s. These larger $\dot{s}_w$ values do not directly affect the afterslip evolution because postseismic slip rates are generally smaller than $\dot{s}_w$.

3.2.2 Coseismic rupture dynamics

The spatially variable coseismic dynamic rupture characteristics of the PM are shown in Fig. 3, together with 90-day aftershock locations (Neves et al., 2022). The PM is more complex than the IM described above. In Movie S1, we provide an animation of the PM's coseismic slip rate evolution to illustrate this complexity. Coseismic rupture separates into two distinct phases set apart by strong deceleration and acceleration of the rupture front. The minimum rupture speed occurs at 5 s rupture time. The PM concentrates slip within several asperities of varying sizes. The first phase of dynamic rupture propagation involves several smaller asperities in the vicinity of the hypocenter. The largest asperity is located in the northwestern part of the fault and ruptures during the second phase. In the northwest, rupture arrest is collocated with where the creeping section of the SAF is inferred to begin. Dynamic rupture is inferred to be pulse-like with high peak slip rates and low rise times during the first phase and transitions to crack-like with lower peak slip rates and high rise times within the large northwestern asperity. The transition from pulse-like to crack-like rupture occurs as the rupture propagates to the northwest, towards the creeping section of the SAF.

3.2.2.1 Seismic moment release and coseismic slip

Fig. 3a shows the moment rate function that consists of two sharply separated peaks with a local minimum at 5 s representing the two phases of the rupture. The on-fault measured moment magnitude of M_w 6.02 corresponds to a seismic moment of $M_0 = 1.33{\times}10^{18}$ Nm, which slightly exceeds the kinematically inferred values that fall between 1.05–1.21$\times10^{18}$ Nm (Liu et al., 2006; Custódio et al., 2009; Twardzik et al., 2012).

The coseismic slip is confined to depths of 4–9 km and extends 3 km in the southeast direction and 20 km in the northwest direction from the hypocenter. The model's average coseismic slip is 39 cm, and the highest values reach approximately 80 cm at several small asperities close to the hypocenter and within the largest asperity 14–19 km northwest of the hypocenter. Rupture extent and asperity locations agree well with previous results from kinematic inversions (Custódio et al., 2009; Twardzik et al., 2012).

3.2.2.2 Stress drop and rupture velocity

The modeled stress drop is spatially highly variable and locally takes negative values. It reaches a local maximum of 21.5 MPa, and its average is 2.7 MPa, which is similar to Ma et al. (2008)'s dynamic rupture model but lower than the value of 4.2 MPa inferred from the lowest misfit model by Twardzik et al. (2014). The highest stress drop values are reached at the asperities close to the hypocenter. Stress drops within the large northwestern asperity do not exceed 9 MPa. 7.9% of the coseismic rupture area exhibits a negative stress drop.

The fault-local rupture velocity shown in Fig. 3d is highly variable. The average local rupture velocity of the PM is 1.4 km/s. This value is the spatial average of rupture speed at each grid point that coseismically slips more than 1 cm and is not equivalent to the average rupture velocity of 1.8 km/s measured from the hypocenter to the northern rupture extent. During the first second of dynamic rupture propagation, it reaches supershear velocity (Freund, 1979; Burridge et al., 1979; Das, 2015) of 4.0 km/s during the nucleation of the rupture, which is unexpectedly slow and below the Eshelby speed. While we do not account for a fault damage zone in our forward simulations, this result of the inversion may reflect the presence of a low-velocity fault zone in Parkfield (Bao et al., 2019). The PM ruptures with an average velocity of approximately 3.0 km/s to the northwest for the next two seconds of rupture time. After breaking through an asperity, the rupture dramatically slows down to speeds slower than 0.8 km/s between 3 and 5 seconds of simulation time. During the second phase, the rupture accelerates again to 2.5 km/s while breaking the large northwestern asperity. After 11 seconds, the rupture slows down until it arrests at 14 seconds after the nucleation. This slow stopping of the rupture leads to a rupture duration exceeding results from other models (Ma et al., 2008; Custódio et al., 2009; Twardzik et al., 2012).

3.2.2.3 Peak slip rate and rise time

The coseismic peak slip rate distribution correlates with the rupture speed distribution (Schmedes et al., 2010; Gabriel et al., 2013). Slip rates reach their highest values of approximately 4.0 m/s around the hypocenter but do not exceed 2.8 m/s within the large northwestern asperity. The spatial average peak slip rate is 1.3 m/s.

Coseismic rise time and peak slip rate are anti-correlated and express distinctly different rupture styles within each rupture phase. We define the coseismic rise time as the duration over which the slip rate exceeds 0.1 m/s. The rise time around the hypocenter is mostly below 1 s in accordance with results from kinematic studies (Liu et al., 2006; Custódio et al., 2009). Rise time is much larger in the northwestern asperity, where it exceeds 3 s.

3.2.3 Seismic and geodetic verification of coseismic rupture dynamics

Fig. 4 shows observed and synthetic seismic waveforms of the PM at the 30 near-field strong-motion stations used to constrain the inversion (Sec. 2.4). We show the max-

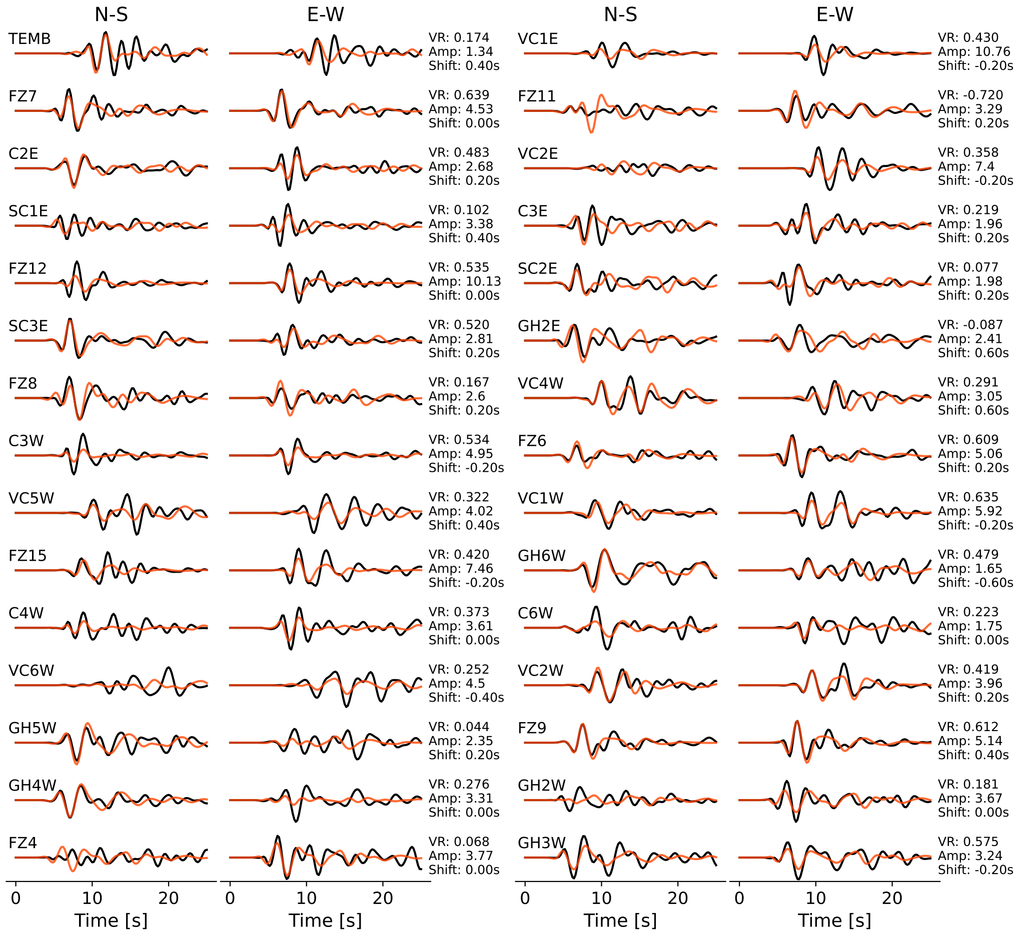

Figure 4. Observed (black, obtained through the CESMD (Center for Engineering Strong Motion Data) web service and operated by the California Strong Motion Instrumentation Program (CSMIP, California Geological Survey, 1972)) and synthetic (orange) seismic velocity waveforms from the PM, bandpass filtered between 0.16–0.5 Hz at the 30 stations used to constrain the inversion. Each waveform (synthetic and observed) is normalized by the respective station's maximum amplitude (Amp, in cm/s, either synthetic or observed maximum). In this Figure, the observed waveforms at each station are cross-correlated and time-shifted relative to the synthetics to maximize the variance reduction (VR) and to account for unmodeled effects of topography and the 3D velocity structure.

imum variance reduction at each station after cross-correlation. However, during the inversion, misfits are calculated without time shifts. The overall variance reduction, calculated from each available seismic data point, is 0.42. We generally fit the onset of the observed seismic waveforms well. The individual stations' variance reductions vary greatly. Station FZ7 exhibits the best individual variance reduction of 0.64. Station FZ11, located nearby, has the worst fit with a strongly negative variance reduction. In general, we cannot identify a clear spatial pattern in the seismic variance reduction (see Fig. S6), except that the three stations closest to the hypocenter, where the modeled dynamic rupture is initiating due to overstress, have a less-than-average variance reduction between -0.09 and 0.18. This suggests that local effects may dominantly cause the misfits away from the hypocenter, e.g., site effects or the fault damage zone with highly variable characteristics along-strike (Lewis & Ben-Zion, 2010). We note that even kinematic source inversions using the same frequency bandwidth struggle to achieve a high seismic variance reduction (Kim & Dreger, 2008).

Fig. 5a shows the observed and synthetic coseismic static horizontal GPS displacements at 12 GPS stations. Synthetic and observed coseismic displacements are compared at 90 s after the rupture onset following Jiang et al. (2021a). The overall coseismic static displacement variance reduction, calculated from each available coseismic displacement data point, is 0.95, which is better than the achieved fit of a kinematic source model constrained by equally weighted seismic strong-motion and GPS data (see Fig. 6b in Kim & Dreger, 2008). The modeled and observed amplitudes and directions fit nearly perfectly at most stations. Our model overpredicts the coseismic displacement at station LOWS, which is located at approximately twice the distance to the fault trace than the second farthest station.

3.2.4 Geodetic verification of postseismic faulting dynamics

Fig. 5b shows the normalized time evolution of the observed and modeled postseismic horizontal displacements at 11 GPS stations that constrain the 90 days of modeled afterslip. Afterslip at all 11 GPS stations is largely steadily increasing, and postseismic displacements after 90 days reach between 1–8 cm on each horizontal component. All components show similar logarithmic decay rates.

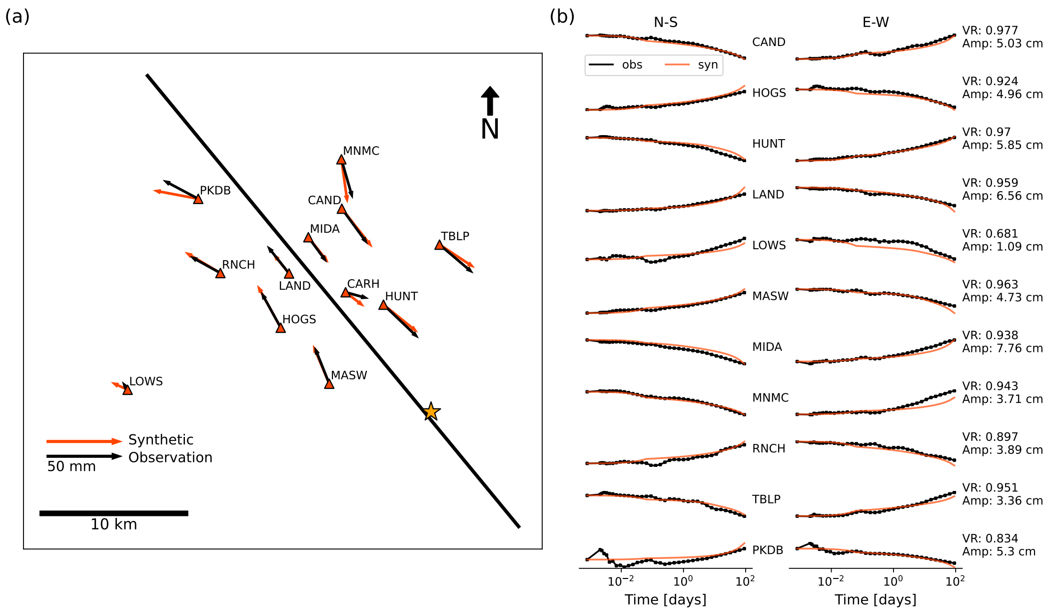

Figure 5. (a) Coseismic horizontal static displacements at 12 GPS stations. Black and orange arrows show observed (Jiang et al., 2021a) and synthetic displacements from the PM, respectively. The black line indicates the model's fault trace and the star marks the epicenter. Both synthetic and observed coseismic displacements are given at 90 s after the rupture onset. (b) Postseismic evolution of the normalized displacements at 11 GPS stations (excluding station CARH) during the first 90 days following the earthquake. Black curves show observations (Jiang et al., 2021a), and orange curves show the synthetics of the PM. The time scale is logarithmic. For each station, we annotate its variance reduction inferred after removing the coseismic displacement and its maximum amplitude.

The PM of our joint dynamic rupture and afterslip inversion captures the first 90 days of observed postseismic GPS deformation well. It achieves an overall variance reduction of 0.94 calculated from each available postseismic data point, which is remarkable for a dynamically consistent joint dynamic rupture and afterslip model. We note that we omit station CARH because it is affected by a polarity change due to slip migrating to the SAF (Sec. 2.4). Similarly to the coseismic displacement misfits, station LOWS has the lowest variance reduction of 0.69. However, its contribution to the overall variance reduction is small due to the small absolute displacement amplitudes at this large distance to the fault. In particular, station PKDB shows spurious oscillations during the first minutes and hours after the earthquake, which probably reflects observational artifacts from an anomalous period of the entire network (Jiang et al., 2021a). We use a logarithmic time scale to accurately sample the early postseismic phase when computing the misfits during the inversion. This leads to a lower implicit weighting of the model's last weeks. For example, we observe a late acceleration of postseismic slip evolution at stations LAND, MASW, and PKDB 50 days after the earthquake in our model but not in observations, which likely reflects this weaker penalty. The GPS stations used in our inversion are expected to resolve shallow slip above the coseismic rupture area accurately. However, their resolution is low at depths larger than 7 km and areas located outside of the lateral extent of the coseismic rupture zone (Page et al., 2009).

Fig. 6a shows the postseismic slip distribution which our PM accumulates during the modeled 90 days of afterslip. The inferred afterslip is mainly confined between the free surface and the coseismic rupture area at 0–5 km depth. Postseismic slip reaches maximum values of 50–60 cm within several slip patches, which is comparable to the maximum coseismic slip. Our model's surface offsets reach 11–17 cm after 60 days, which agrees well with surface offsets ranging from 12-20 cm measured on alignment arrays (Lienkaemper et al., 2006). Considerable parts of the fault that slipped coseismically continue to host afterslip. Afterslip can reach up to 35 cm within areas that slipped coseismically, which is almost half of the maximal inferred coseismic slip. Overall, the postseismic slip evolution reflects a smooth transition from the co- to the postseismic phase supported by employing the same friction law.

A striking feature of the model's afterslip distribution is a pronounced gap in the afterslip located directly above the coseismic rupture area approximately 7–8 km northwest of the hypocenter. Such a local lack of slip is also present in the postseismic slip

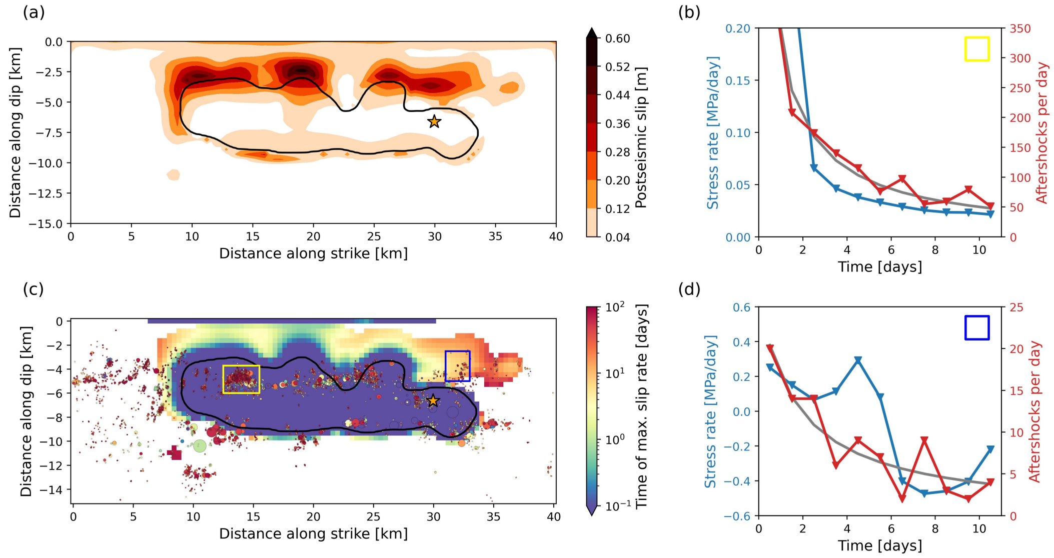

Figure 6. (a) 90-day postseismic slip of the PM. The black contour shows the extent of the coseismic rupture, and the star marks the hypocenter. (b) Aftershock rates (red) compared to average stress rates (blue) of our PM within the yellow aftershock clusters marked in (c). The grey curve shows Omori's law ($n(t) = \frac{k}{c+t}$) fitted to the aftershock rates with $c = 0.68$ days and $k = 534.4$, where n represents the daily frequency of aftershocks depending on the time t since the mainshock. (c) Time evolution of the postseismic rupture front defined as the time of the maximum postseismic slip rate of each point where the maximum slip rate is higher than 10^{-8} m/s. The plate rate is approximately 10^{-9} m/s (Lisowski et al., 1991). Aftershock locations (Neves et al., 2022) are annotated and colored by the same logarithmic color scale, and their size is proportional to their seismic moment. The yellow and dark blue rectangles outline two aftershock clusters for which we compare aftershock rates and mean stress rates in (b) and (d). (d) Same as (b) for the aftershock cluster located within the dark blue rectangle marked in (c). Omori's law is fitted using $c = 1.78$ days and $k = 46.51$.

model of Murray and Langbein (2006). In our PM, the same area that features a gap in the afterslip acts as a strong barrier to the coseismic dynamic rupture propagation and causes strong rupture deceleration starting at 3 seconds after the nucleation (Fig 3b). As mentioned before, the minimum coseismic rupture speed is reached at 5 s propagation time.

3.2.5 Kinematics of afterslip and aftershocks

Fig. 6c shows the temporal evolution of the maximum postseismic slip rate and 90-day aftershock activity following the earthquake (Neves et al., 2022). During the first three hours after the earthquake, an afterslip front develops at the shallow perimeter of the coseismic rupture and migrates up to 2 km above the coseismic slip. Surface afterslip, possibly aided by locally low confining stress in our forward models, also initiates during the first two hours after the earthquake (Langbein et al., 2005) but is initially not connected to the afterslip front migrating away from the coseismic rupture area. The fastest afterslip front is located 12 km northwest of the hypocenter and reaches the surface approximately one day after the earthquake. All major afterslip patches reach their maximum slip rate during the first 10 days following the mainshock. A small afterslip patch southeast of the hypocenter spontaneously emerges 10 days after the event and later connects to an afterslip front originating from the coseismic rupture area. The maximum modeled slip rate within this emerging afterslip patch reaches 10^{-6} m/s. However, the afterslip inferred at the southeastern part of the fault has a higher uncertainty as the sensitivity of the GPS network is lower (see Sec. 3.3.1 and Page et al., 2009).

Aftershock locations are related to the coseismic slip distribution. At the bottom and the lateral sides of the coseismic rupture area, aftershocks are mostly located at the edge or outside of the coseismic rupture area. A band of aftershocks, including the most active clusters, occurs mostly within the coseismic rupture zone between 4–6 km depth. Below 6 km depth, the coseismic rupture area is widely depleted of aftershocks reflecting coseismic stress release.

To analyze the spatiotemporal relationship between afterslip and aftershocks, we compare afterslip stressing rates and aftershock seismicity evolution with time. Figs. 6b,d show aftershock rates of two aftershock clusters during the first 10 days after the mainshock. The aftershock rate of the largest aftershock cluster (yellow rectangle) compares well to our model's mean stressing rate within the cluster region. The decay of the aftershock rate n with time since the mainshock t follows Omori's law ($n(t) = \frac{k}{c+t}$, grey curve in Fig. 6b) with $c = 0.68$ days. The inferred c value in this area falls within the typical range of 0–1 days and is often associated with incomplete detection of small events (Utsu et al., 1995; Kagan & Houston, 2005).

Aftershocks located within the blue rectangle in Fig. 6c may be driven by an afterslip front that arrives 5–6 days after the mainshock. This afterslip front originates 4 km northwest from the hypocenter and propagates backward in the southeast direction. The average stressing rate within this region shows considerable complexity due to the passage of the afterslip front. The average stress rate decreases during the first days after the mainshock. However, after 3 days, it starts to increase again, peaking at 4.5 days, which is aligned with the arrival of the afterslip stress front. Then, the stress rate rapidly decreases and turns negative due to the stress release caused by the passing afterslip. This may explain the observed considerable aftershock increase 7.5 days after the mainshock, which coincides with the maximum negative stress rate in our model. It is difficult to apply Omori's law to this aftershock cluster. To match the aftershock rate peak at 7.5 days, an unusually large c value of 1.78 is required. Removing the peak reduces c to 1.54, which is yet larger than typical values.

Fig. 7a shows the afterslip rise times of the PM, which vary by more than two orders of magnitude. Within the coseismic rupture area, afterslip rise times are short and range between a few hours to a few days. Outside the coseismic rupture area, afterslip rise times rapidly increase to weeks and months. This increase gradually occurs over a distance of approximately 2 km away from the edge of coseismic rupture.

An interesting exception is a localized, approximately 4 km wide region above the hypocenter, where afterslip rise time remains constant between 15–20 days. Afterslip in this epicentral region originates from 4 km northwest along-strike from the hypocenter. There, coseismic rupture penetrates the shallow velocity-strengthening zone and initiates an afterslip front that propagates with constant rise time in the backward direction of coseismic rupture. This afterslip front propagates at a speed of approximately one kilometer per day, which is comparable to rupture velocities of slow slip events (e.g., Vavra et al., 2023). This afterslip front may drive aftershock activity (Fig. 6c and Movie S2).

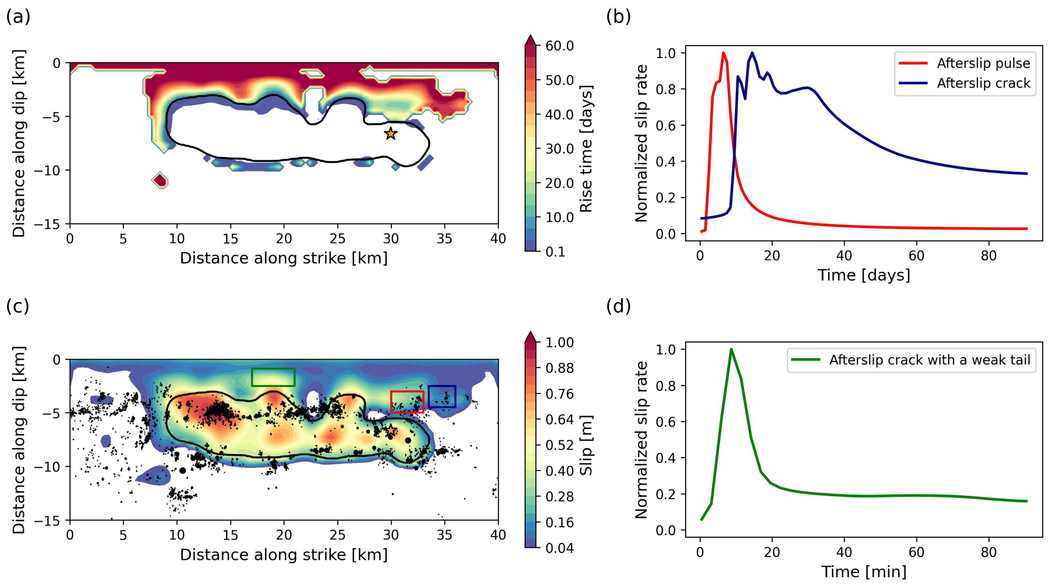

Figure 7. (a) Afterslip rise times defined as the time it takes to reach 80% of the final slip. (b) Normalized average slip rates within the red and blue rectangle marked in (c). (c) Combined coseismic slip and 90 days of postseismic slip of the PM. Colored rectangles indicate regions for which mean slip rates are shown in subplots b and d. The black line indicates the extent of the coseismic rupture, black dots show aftershock locations, and the star marks the hypocenter. (d) Normalized average slip rate within the green rectangle marked in (c).

The afterslip in our rate-and-state framework takes the form of different rupture styles resembling coseismic pulse-like and crack-like rupture across the same fault. The red curve in Fig. 7b shows a pulse-like afterslip slip rate function associated with the afterslip region within the red rectangle in Fig. 7c, where the backward propagating afterslip front is located. The average slip rate function of the adjacent region marked with a blue rectangle (blue curve in Fig. 7b) reveals a distinctly different slip rate behavior. Here, the slip rate function resembles a crack-like style of afterslip, remaining above 35% of the peak slip rate until the end of the 90-day simulation time. This region represents a coalescence of two afterslip fronts, the first arriving from the northwest region marked in red and the second originating from the spontaneously emerging afterslip patch to the southeast. However, the latter feature is associated with considerable uncertainties (see Sec. 3.3.1) and falls within the low GPS sensitivity fault region.

The green curve associated with the fault segment marked by a green rectangle (Fig. 7c,d) shows the normalized mean slip rate function of the area with the maximum afterslip. The time scale of the afterslip in the region marked in green (minutes) differs from the time scales of the afterslip in the regions marked in red and blue (days). The associated time scales rapidly increase with distance to the extent of the coseismic rupture. This slip rate function resembles an intermediate afterslip style falling in between a pulse-like and crack-like characteristic. It is characterized by a sharper peak in the beginning and a weaker tail remaining at approximately 20% of the peak slip rate.

3.2.6 Strength excess and fracture energy

Fig. 8 shows the initial strength excess ($\tau_y - \tau_0$, with $\tau_y = f_0\sigma_n$) and the coseismic fracture energy distribution of our PM. The strength excess distribution implies two fundamentally different coseismic rupture-stopping mechanisms. The strength excess within the coseismic rupture area is generally low, with a spatial average of 1.05 MPa. It contains negative values. Shallow coseismic rupture is partly terminated at local fault strength 'barriers', marked with blue lines in Fig. 8a, which are areas with larger strength excess than their surroundings (Pulido & Dalguer, 2009). In distinction, coseismic rupture stops in regions with negative strength excess at three shallow locations (yellow lines in Fig. 8a). We calculate the yield stress τ_y using the reference friction coefficient to approximate the static fault strength (see Sec. 4.4). However, the maximum friction coefficient reached during rupture is not a fixed, prescribed parameter of our forward model. In our

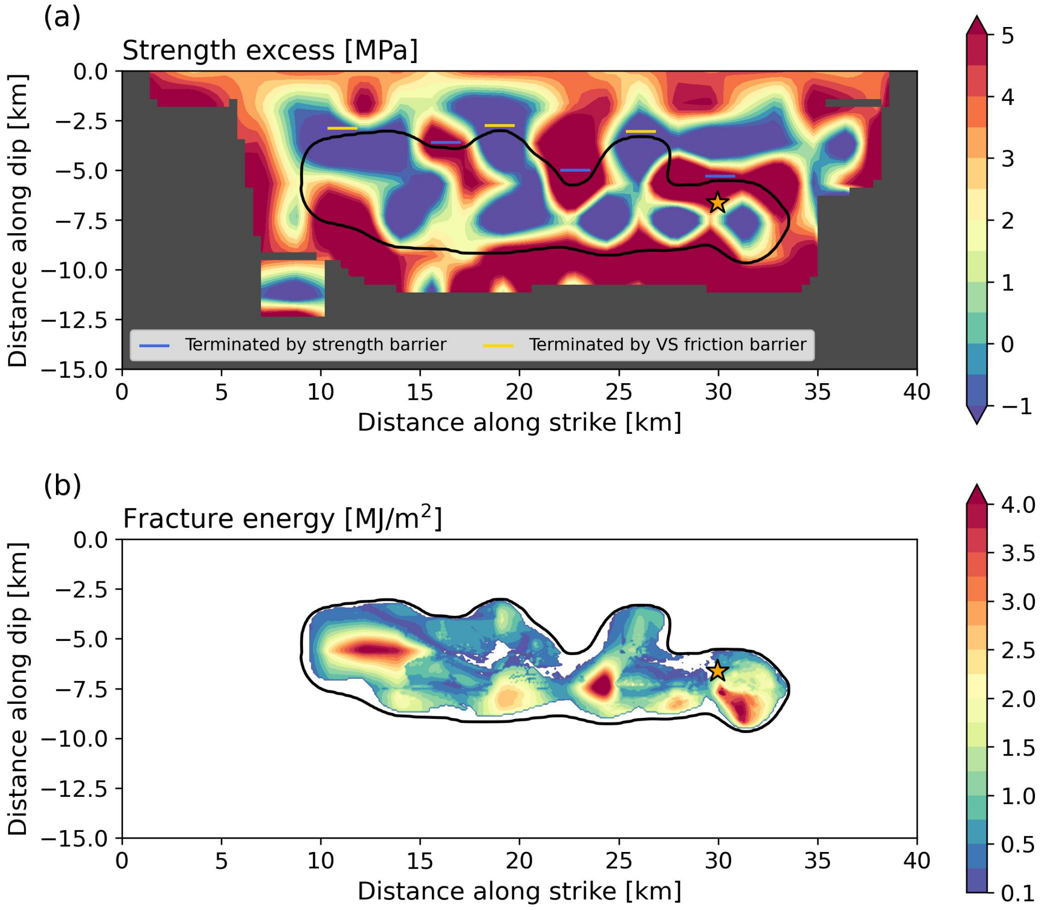

Figure 8. PM's (a) initial strength excess ($\tau_y - \tau_0$), (b) coseismic fracture energy distributions. We only show the strength excess where coseismic and postseismic slip combined exceed 10 cm somewhere within a radius of 1.2 km, which we consider as constrained by the inversion.

simulations, the reference friction coefficient represents a lower bound of static friction within the velocity-weakening regions (Ulrich et al., 2019).

We find that fracture energy is correlated with stress drop distribution (Fig. 3c). We define fracture energy per unit area as:

$$\mathrm{G} = \int_0^{x_{\tau_{min}}} [\tau(x) - \tau_{min}]\, dx, \tag{9}$$

where τ is shear stress, x is slip, $\tau_{min}(\approx \tau_d)$ is minimum shear stress, and $x_{\tau_{min}}(\approx L)$ is slip at the minimum shear stress. The three regions with the largest fracture energy are located (i) southeast below the hypocenter, (ii) 7 km northwest of the hypocenter, where dynamic rupture decelerates abruptly, and (iii) within the large asperity 15 km northwest of the hypocenter. The spatial average of the fracture energy within the coseismic rupture area is 0.95 MJ/m^2. Our inference here is similar to the 1.1 MJ/m^2 inferred for the similarly-sized 2016 M$_w$ 6.2 Amatrice normal faulting event (Gallovič et al., 2019b). A smaller value of 0.044 MJ/m^2 has been recently inferred from earlier 3D dynamic rupture models of a sequence of small (M$_w$ 1.9) repeating earthquakes on the SAF 25 km northwest to the 2004 Parkfield hypocenter (Lui & Lapusta, 2018; Gabriel et al., 2023), in line with the observed fracture energy scaling with earthquake - or rupture - size (Cocco et al., 2023; Gabriel et al., 2023).

3.3 Model ensemble characteristics and dynamic parameter trade-offs

To assess model uncertainties and trade-offs, we analyze model average quantities and their variability obtained from an ensemble of best-fitting models (Sec. 2.6) containing 10,500 unique model parameterizations. The ensemble average distributions of slip, rise time, afterslip, and dynamic parameters are similar to the ones of the PM. The separation into two coseismic rupture phases with different rupture styles and the locations of co- and postseismic slip asperities are stable features of the model ensemble.

3.3.1 Ensemble averages and uncertainties

Fig. 9 shows the best model ensemble's average and standard deviation of the coseismic slip, the rise time, and the afterslip. The mean coseismic slip distribution is very similar to the slip distribution of the PM. Its spatial median coefficient of variation is

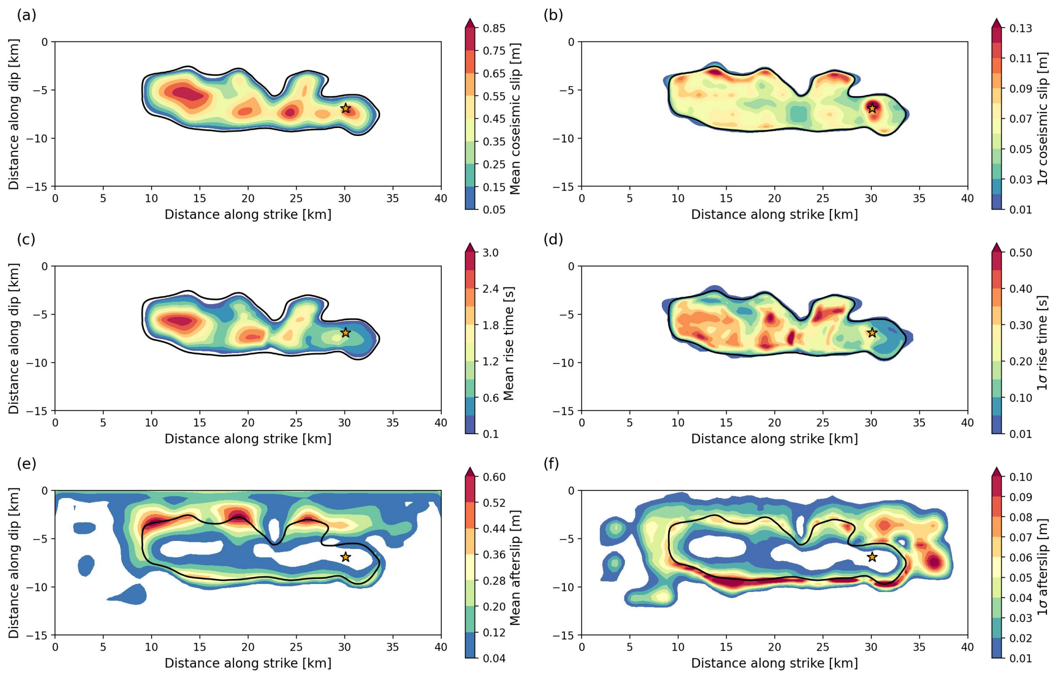

Figure 9. Ensemble average (a) coseismic slip, (c) rise time, (e) postseismic slip, and their respective standard deviations (b,d,f). Averages and standard deviations are computed from the best-fitting model ensemble containing 10,500 unique models.

17.3%. The standard deviation distribution has its lowest values 8 km northwest of the hypocenter, where the rupture strongly decelerates. This illustrates that this rapid rupture deceleration is a critical phase of the coseismic rupture dynamics. Large standard deviation values are mostly concentrated close to the rupture edges. They reach particularly high values where the rupture terminates due to the transition to the velocity-strengthening regime, indicating that the abruptness of rupture termination depends on the stopping mechanism. The locally high standard deviation of the rupture contours at the same location (Fig. S7) confirms this observation.

The mean rise time distribution shows short rise times around the hypocenter and an area with increased rise times at the northwestern end of the rupture. The coefficient of variation of both rise-time features lies in the range of 10–20%, indicating that they are stable results of the inversion. The rise time standard deviation distribution reaches its largest value approximately 9 km northwest of the hypocenter, where the rupture accelerates again after nearly terminating.

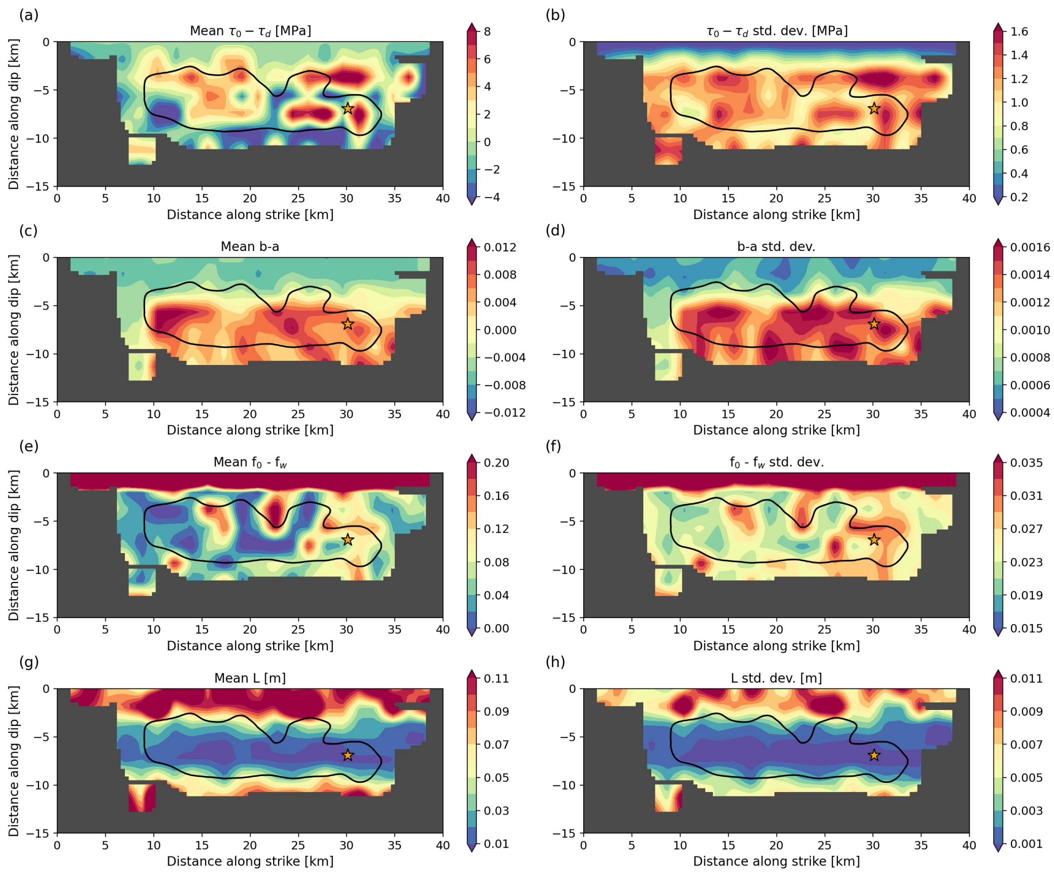

Figure 10. Mean distributions of the best-fitting model ensemble's (a) potential stress drop $\tau_0 - \tau_d$, (c) $b - a$, (e) reference friction drop $f_0 - f_w$, (g) characteristic weakening distance L, and their respective standard deviations (b,d,f,h). The model ensemble contains 10,500 models. We mask areas where the sum of coseismic and postseismic slip does not exceed 10 cm within an area of a radius of 1.2 km, which we consider unconstrained.

The afterslip variability is greatest at the bottom of the coseismic rupture zone, reflecting the combined effects of varying rupture extent and the GPS network's low resolution. Another zone of high afterslip variability above and southeast of the hypocenter likely reflects the weak constraints due to the GPS network configuration, with all stations located northwest of the hypocenter. The variability is generally reduced close to the free surface, where the sensitivity of the GPS network increases.

The dynamic parameters do not vary extensively within the ensemble. Figure 10 shows the ensemble mean and the standard deviation distributions of the potential stress drop $\tau_0 - \tau_d$, $b - a$, the reference friction drop $f_0 - f_w$, and the characteristic weakening

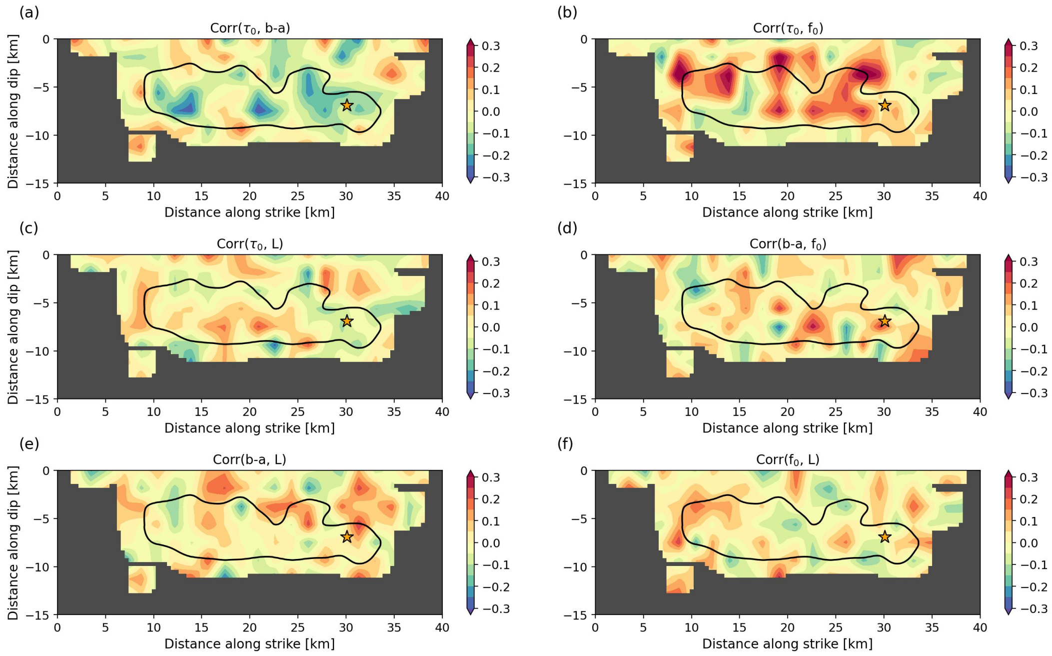

Figure 11. Ensemble correlation coefficients' spatial distribution of dynamic parameter pairs (a) τ_0 and $b-a$, (b) τ_0 and f_0, (c) τ_0 and L, (d) $b-a$ and f_0, (e) $b-a$ and L, (f) f_0 and L. The black contour indicates the extent of the coseismic rupture, and the star marks the hypocenter. We mask areas where the sum of coseismic and postseismic slip does not exceed 10 cm within an area of a radius of 1.2 km, which we consider unconstrained.

distance L. The means of all four dynamic parameters are comparable to the PM (see Fig. 2). The standard deviations are relatively small and highly correlated with the corresponding mean distributions. Plotting the coefficient of variation of the four dynamic parameters or a strictly positive equivalent (see Fig. S8) confirms this observation. The coefficients of variation of all four parameters are spatially rather homogeneous, with values ranging mostly between 4–8%. Within the coseismic rupture area, τ_0 has the smallest and L the largest relative uncertainties.

3.3.2 Ensemble correlations and source parameters

The prestress is locally (anti-)correlated with $b-a$ and f_0, while overall correlation values between different dynamic parameters are small. Fig. 11 shows correlation coefficients of the ensemble's dynamic parameters to analyze trade-offs between them. Correlation coefficients rarely exceed ± 0.4. Locally, prestress τ_0 and reference friction coefficient f_0 share the highest positive correlation. Maximum values up to 0.4 are reached in areas where coseismic and postseismic slip overlap, likely because prestress variations can be dynamically balanced by changes in the reference friction coefficient. τ_0 and $b-a$ show an anticorrelation of up to -0.3. High anticorrelation in areas with large rise times may indicate that a careful balance between τ_0 and $b-a$ is important to facilitate sustained crack-like rupture. Slip-weighted average correlation coefficients of the other four parameter pairs are below 0.02.

The dynamic source inversion approach facilitates computing fundamental earthquake source parameters such as radiated energy and fracture energy while simultaneously relying on observed data and the underlying physics. Fig. S9 displays histograms of various coseismic and postseismic rupture parameters of the best-fitting model ensemble. We find an ensemble average radiated energy of 2.19×10^{13} J and an average coseismic fracture energy of 8.30×10^{13} J, which translates to an average radiation efficiency of 21%.

4 Discussion

4.1 Mixed crack- and pulse-like rupture dynamics governed by local fault heterogeneity

It remains debated whether earthquakes predominantly propagate as cracks or as pulses (Heaton, 1990). For example, Lambert et al. (2021) hypothesize that large megathrust events mainly rupture as 'mild' cracks whereas crustal strike-slip faults rupture in the form of self-healing pulses. We infer a clear transition from pulse-like (short rise time) to crack-like (long rise time) coseismic rupture of the crustal strike-slip 2004 Parkfield earthquake. This may indicate that the style of earthquake rupture rather depends on local rheological and frictional properties than on the regional tectonic setting and that one earthquake may comprise more than one rupture style (e.g., Gabriel et al., 2012).

We analyze the spatial correlation between rise times and dynamic parameters (Fig. S10) of our preferred model (PM) to understand the underlying factors causing the coseismic rupture style transition. While rise time does not correlate with the potential stress drop $\tau_0-\tau_w$, it depends on the interplay between f_0-f_w, $b-a$, and L. The reference friction drop exhibits the highest (anti-)correlation of -0.59 with rise time. The largest rise times are reached when the reference friction drop is smaller than 0.05. L

shows an anticorrelation (-0.39) with rise time and $b - a$ shows a positive correlation of 0.47 with rise time. These results imply that a velocity-weakening regime, with small L and small $f_0 - f_w$, promotes crack-like rupture. Contrary to our results, Ampuero and Rubin (2008) report an anticorrelation between $b - a$ and rise time. The overall geometrical simplicity of the Parkfield segment suggests that the observed rupture behavior is driven mainly by initial stresses and specific local frictional properties. We conclude that it's a complex interplay of fault-local dynamic parameters that likely determines the rupture style.

In our PM, both rupture styles produce vastly varying seismic radiation. Fig. S11 shows a waveform comparison with synthetics generated by a 5 s version of our PM, including only the initial pulse-like phase. The short model's overall seismic variance reduction reaches 95.3% of the full model's variance reduction, but the short model cannot explain the displacements measured by the GPS stations. The initial pulse-like phase produces most of the seismic radiation while accounting only for 35.7% of the seismic moment, in agreement with observations (Allmann & Shearer, 2007).

This is consistent with our inferred gradual transition from the coseismic to the postseismic phase. Coseismic rupture dynamics initiate as a strongly radiating phase, followed by a mildly radiating phase, which only weakly imprints on the seismic data but produces dynamic perturbations in the GPS data (Jiang et al., 2021a). Finally, aseismic afterslip dominates with rise times increasing with time and distance from the coseismic rupture area (Fig. 7). These results highlight the importance of complementary data sets to infer kinematic and dynamic source models and have important implications for seismic hazard assessment: Similarly sized earthquakes can cause vastly different ground motions based on the dominantly operating rupture style, and large earthquakes can experience strong local amplifications due to dynamic rupture complexity (Schliwa & Gabriel, 2023).

4.2 Early supershear and rupture speed variability

We observe locally pronounced rupture speed variations in our dynamic rupture inversion. While our models are based on low-frequency data, our results may explain locally observed high-frequency radiation. Similar to the rupture speed in our PM, Custódio et al. (2009) reported a supershear rupture onset with velocities above 4 km/s during the first second of their kinematic source model. However, their model does not feature strong rupture deceleration after 3 seconds, although the final slip distribution is similar to our model. Fletcher et al. (2006) determined the rupture velocity of the 2004 Parkfield earthquake via back-projection using a short-baseline array 12 km west of the epicenter. They also inferred a fast rupture onset but without reaching supershear speeds. In their study, the rupture starts with a velocity of 3.3 km/s and then drops to an average velocity of 2.4 km/s.

Allmann and Shearer (2007) found a burst of high-frequency seismic radiation originating at the southern edge of the northern high-slip patch approximately 13 km northwest of the hypocenter and 5.5 s after rupture initiation. Our model ensemble persistently features a strong rupture deceleration and subsequent acceleration between the southeastern and northwestern parts of the rupture. Such abrupt changes in rupture velocity cause high-frequency radiation (e.g., Madariaga, 1977; Shi & Day, 2013; Schliwa & Gabriel, 2023). The rupture speed change in our model ensemble is caused by a strong fault strength barrier (Fig. S12a) that extends from 8–3 km depth and also creates an afterslip gap (Fig. 9e). This barrier is a well-constrained feature of our model and might represent a local rheological or geometrical complexity.

Fletcher et al. (2006) tracked high-frequency arrivals with a short-baseline seismic array located about 12 km west of the Parkfield epicenter. They also observe strong high-frequency sources where our rupture models abruptly decelerate after the impulsive initial phase. However, they do not find any high-frequency sources at the northwestern large slip patch, which is compatible with our modeled mildly radiating crack-like rupture.

4.3 Dynamic rupture arrest

We find that distinct dynamic rupture-stopping mechanisms of different parts of coseismic rupture correlate with locally distinct afterslip evolution.

During dynamic rupture, elastic strain energy release competes with the consumption of fracture energy (Ke et al., 2018; Barras et al., 2023; Cocco et al., 2023). On a planar fault, dynamic rupture terminates if (i) it dynamically runs out of available strain energy; or (ii) local changes in normal stress or frictional conditions increase the required fracture energy or lead to velocity-strengthening conditions. At three shallow locations (yellow lines in Fig. 8a), coseismic rupture stops in regions with negative strength excess. Comparing the coseismic rupture contours with the $b-a$ distribution (Fig. 2b) reveals that dynamic rupture terminates at these locations because it enters velocity-strengthening regions. Later, these three locations form the origin of main afterslip patches (Fig. 6a). There is no or very little afterslip evolving in regions where coseismic rupture is stopped due to local strength excess barriers.

The dynamic parameters L and $\dot{s}_w$ additionally contribute to the dynamic rupture arrest. When coseismic rupture propagates into velocity-strengthening parts of the fault, slip rates cannot reach the locally increased $\dot{s}_w$ values anymore (Fig. 2e), accelerating the rupture arrest. L noticeably increases above and beneath the coseismic rupture area (Fig. 2d). However, rupture arrest in the along-strike direction is not associated with an increase of L.

4.4 Coseismic stress drop, friction drop and implications for the heat flow paradox

Our modeled low average coseismic stress drop may reflect the Parkfield section's comparably short recurrence times. The PM's average on-fault measured coseismic stress drop is 2.76 MPa which is rather small. We compare the on-fault dynamic stress drop to a seismological Brune-type stress drop estimate from calculating the average stress drop from the moment rate function spectrum using the following equation (e.g., Kaneko & Shearer, 2014):

$$\Delta\sigma_{e_f} = \frac{7}{16}\left(\frac{f_c}{k\beta}\right)^3 M_0\,, \tag{10}$$

where $f_c = 0.156$ Hz is the corner frequency of a Brune spectrum (Brune, 1970) fitted to the moment rate function spectrum of the PM (Fig. 3a), $\beta = 3600$ m/s the average S-wave velocity, $M_0 = 1.33 \times 10^{18}$ Nm the seismic moment, and k is a constant depending on the assumed source model. The resulting $\Delta\sigma_{e_f} = 2.72$ MPa reproduces the average on-fault stress drop when assuming $k = 0.26$, which is the value for S-wave spectra of the cohesive-zone model by Kaneko and Shearer (2014). Allmann and Shearer (2009) found that moderate to large strike-slip earthquakes have a median stress drop of 10 MPa when assuming the Madariaga (1976) source model. We infer $\Delta\sigma_{e_f} =$ 5.16 MPa when using $k = 0.21$ from the Madariaga source model, which is approximately half of the 10 MPa median value that Allmann and Shearer (2009) inferred for moderate to large strike-slip earthquakes.

The SAF is a mature fault system that is assumed to operate under relatively low absolute stress levels based on the absence of a heat flow anomaly (e.g., Lachenbruch & Sass, 1980; Rice, 1992; Williams et al., 2004) and borehole measurements at the San Andreas Fault Observatory at Depth (e.g., Hickman & Zoback, 2004). The absence of a heat flow anomaly above the SAF may be explained by statically strong and dynamically weak faults due to strong dynamic weakening at coseismic slip rates or by an effectively low static fault strength with respect to Byerlee's law (Byerlee, 1978). A statically weak SAF may be caused by weak fault gouge (Lockner et al., 2011) or elevated pore fluid pressure (Rice, 1992).

Using a friction law with a rapid-weakening mechanism at coseismic slip rates allows faults to operate at low average shear stress (Noda et al., 2009; Ulrich et al., 2019). Our PM exhibits a small average reference friction drop of 0.058 within the coseismic rupture area, which would not align with the concept of statically strong and dynamically weak faults. However, our model parameter, the reference friction drop, is not necessarily representative of the effective friction drop. The low-velocity steady-state friction f_{LV} depends on the initial slip rate $\dot{s}_{init}$, the reference slip rate $\dot{s}_0$, and $b-a$ (see Eq. 5). The maximum friction coefficient reached during rupture is not a prescribed model parameter but varies along the fault and often exceeds f_0, but rarely falls below this value. We measure $f_{max} = \tau_{max}/\sigma_0$, where τ_{max} is the maximum shear stress at a given point on the fault, to analyze the static fault strength in the preferred model and find $f_{max} = 0.66$ on average within the VW regions of the coseismic rupture area, which results in an effective friction drop $f_{max}-f_w$ of on average 0.36. This larger effective friction drop is yet smaller than expected from Byerlee's law and a lithostatic pressure gradient.

We note that our ensemble of dynamic rupture models might be biased by the choice of the initial model (IM), which has an even smaller average reference friction drop. Although we cannot exclude that an alternative dynamic rupture model with a different reference friction drop may fit the data, the construction of the IM (Sec. 3.1) demonstrates that considerably larger fracture energy is likely incompatible with the earthquake's large-scale rupture properties. The comparably small average coseismic characteristic weakening distance of 3 cm is approximately 25% of the expected value considering the earthquake's magnitude and rupture size (Gabriel et al., 2023; Palgunadi et al., 2024). As we cannot achieve a higher reference friction drop without a shorter weakening distance while preserving fracture energy, we consider a higher friction drop dynamic model unlikely to be mechanically viable.

4.5 Negative coseismic stress drop may promote afterslip and aftershocks

In our PM, 7.9% of the coseismic rupture area exhibits a negative coseismic stress drop. We find that the largest connected area of negative coseismic stress drop at 12–13 km northwest to the hypocenter (Fig. 3c) coincides with the area of most afterslip within the extent of the coseismic rupture (Fig. 6a). Mikumo and Miyatake (1995)'s dynamic rupture model of the 1984 Morgan Hill earthquake featured negative stress drops to explain small slip over a shallow fault section, which they associated with velocity-strengthening behavior (Quin, 1990; Blanpied et al., 1991). Similar to Mikumo and Miyatake (1995)'s model, our results include a small average strength excess, which likely promotes negative stress drops. Using dynamic-weakening friction, Noda and Lapusta (2010) inferred regions of negative stress drop also for velocity-weakening areas with slip larger than the average slip.

We observe that areas of negative stress drop align with increased aftershock activity. Custódio et al. (2009) found that aftershocks tend to occur in regions of negative stress change in a stress change model inferred from a kinematic slip model. Here, we observe an interesting relationship between the aftershock locations and the slip distribution of our PM, which is compatible with this observation. At the bottom and the lateral edges of the coseismic rupture area, aftershocks are mostly located outside of the coseismic rupture area (Fig. 6c), where a stress increase is expected (Fig. S13). In contrast, the shallow aftershock clusters between 4–6 km depth occur still within the coseismic rupture zone, where a static stress change model would produce a negative stress change. In our rate-and-state friction model, shallow rupture is often stopped by velocity-strengthening friction. The shallow aftershocks coincide with the transition from a velocity-weakening to a velocity-strengthening regime (Fig. 2b). Our model demonstrates that this transition zone can exhibit a considerable area of negative stress drop, which is compatible with increased aftershock activity.

4.6 Limitations of this study

Our 90-day afterslip simulation does not account for viscoelastic effects. Freed (2007) suggest that the 2004 Parkfield postseismic deformation was solely caused by afterslip, and viscoelastic relaxation and poroelastic rebound had no significant contribution. In distinction, Bruhat et al. (2011) argue that viscoelastic relaxation is required to explain as much as 20% of the postseismic displacement at the GPS station farthest from the source (LOWS, see Fig. 1a) 5 years after the earthquake. Based on their analysis, the contribution of viscoelastic relaxation to near-source displacements during the early post-seismic time may be negligible (see Fig. 8b in Bruhat et al., 2011).

Albeit running more than 2 million dynamic rupture forward simulations, our inversion visits only a tiny portion of the large model space associated with ≈ 1100 dynamic parameters. Our inverse problem also has a large null space because wide parts of the fault do not slip significantly. By providing a reasonable IM and guiding the inversion during the convergence phase by occasionally selecting our preferred model and restarting all Markov chains with the chosen model, we were able to find an ensemble of models that explains the coseismic and postseismic data, which is a similar approach to previous studies (Gallovič et al., 2019b; Premus et al., 2022). However, our best-fitting model ensemble cannot be assumed to be completely independent of the initial model. While the model uncertainties that we provide represent ranges of parameters that can fit the data, we cannot expect that the uncertainty quantification is mathematically complete in a Bayesian probabilistic sense.

The overall similarity between models within the ensemble may bias the absolute correlation coefficients. We find that the correlations between the different dynamic parameters of the ensemble (Fig. 11) are generally low (< 0.5). However, the correlation coefficients of the best-fitting model ensemble increase with the length of the Markov chains and might rise further when the inversion is continued.

The earthquake dynamic inversion problem suffers from the so-called "curse of dimensionality" - the volume of the parameter space exponentially increases with the number of parameters. Further increasing the computational resources consumed (>57,000 GPU hours for this study) will likely be impermissible or at least highly inefficient because the error of the MCMC results decreases more slowly with the number of steps (Sokal, 1997).

Instead, future methodological improvements may be achieved by either (i) the introduction of advanced methods or (ii) reducing the number of model parameters. With respect to (i), new methods such as reduced-order modeling and machine learning techniques may aid in considerably speeding up the forward model (Rekoske et al., 2023). Physics-based neural networks were recently applied to the rupture problem with rate and state friction and allow for dynamic parameter estimation as part of the training process (Rucker & Erickson, 2023). Recently, Stiernström et al. (2024) derived an adjoint-based inversion formulation for dynamic rupture, which may reduce the time-to-solution of dynamic source inversions but cannot provide model uncertainties. For (ii), reducing the number of control points by, e.g., decreasing their density at the edges of the fault or places with no expected slip will decrease the dimensionality of the forward problem. Similarly, using a simpler linear-slip weakening friction law requires fewer model parameters and computational resources but can only capture coseismic rupture dynamics (e.g., Gallovič et al., 2019b).

5 Conclusions

In this study, we conduct a joint dynamic rupture and afterslip finite-fault inversion of the 2004 M_w 6.0 Parkfield earthquake, resolving the spatial variability of prestress and fault friction parameters across time scales. Using the best-fitting model ensemble, we delineate the uncertainty bounds of dynamic model parameters and reveal their inherent trade-offs. The preferred dynamic model unifies the complexities of co- and postseismic fault slip, jointly constrained by seismic and geodetic observations. We observe significant spatial heterogeneity in coseismic dynamic rupture and identify a pulse-like rupture phase followed by a crack-like rupture phase. Two distinct coseismic rupture phases are separated by a shallow strength barrier located 7–8 km northwest of the hypocenter, which nearly arrests coseismic slip and subsequently causes a pronounced gap in the 90-day afterslip evolution. Our joint rate-and-state framework elucidates distinct dynamic rupture termination mechanisms, which are closely tied to the subsequent evolution of afterslip. Across the entire area of fault slip, including regions hosting afterslip, the spatial average of $b-a$ levels at 0.000 (with a standard deviation of 0.0059). Postseismic slip rate functions mostly resemble crack-like behavior with rise times gradually increasing with distance to the edge of the coseismic rupture area. We detect a backward propagating afterslip front, which aligns with delayed aftershock activity located above the hypocenter. Our analysis provides data-constrained and physics-based estimates of source parameters and their interactions. We observe areas of negative coseismic stress drop that may explain the occurrence of shallow aftershock clusters within the coseismic rupture area. The inferred friction drop aligns with a statically stronger and dynamically weaker Parkfield section of the San Andreas Fault. The 10,500 best-fitting model ensemble's average coseismic radiation efficiency is 0.21, its coseismic stress drop is 2.73 MPa, and its average postseismic stress drop is 0.39 MPa, despite similarly large co- and postseismic moments. This study demonstrates how physics-based models using modern computational techniques can uncover new insights and unprecedented details of well-recorded earthquakes.

6 Open Research

All seismic data are obtained through the CESMD (Center for Engineering Strong Motion Data) web service and we only use stations from the California Strong Motion Instrumentation Program (CSMIP, California Geological Survey, 1972). We use processed coseismic and postseismic GPS data by Jiang et al. (2021a), which are publicly available: `https://doi.org/10.5281/zenodo.4278477` (Jiang et al., 2021b). The FD3D_TSN (Premus et al., 2020) version and all required input files to run the dynamic source inversion of the 2004 Parkfield earthquake are available here: `https://doi.org/10.5281/zenodo.11072717` (Schliwa, 2024).

Acknowledgments

The authors declare no conflict of interest. This study was supported by the European Union's Horizon 2020 Research and Innovation Programme (TEAR, grant number 852992), Horizon Europe (ChEESE-2P, grant number 101093038, DT-GEO, grant number 101058129, and Geo-INQUIRE, grant number 101058518), the Deutsche Forschungsgemeinschaft (DFG, German Research Foundation, grant number 495931446), the National Aeronautics and Space Administration (80NSSC20K0495), the National Science Foundation (grant numbers EAR-2225286, EAR-2121568, OAC-2139536, OAC-2311208) and the Southern California Earthquake Center (SCEC awards 22135, 23121). F. G. was supported by the Johannes Amos Comenius Programme (P JAC), project No. CZ.02.01.01/00/22_008/0004605, Natural and anthropogenic georisks. Computing resources were provided by the Institute of Geophysics of LMU Munich (Oeser et al., 2006).

References

Allmann, B. P., & Shearer, P. M. (2007). A High-Frequency Secondary Event During the 2004 Parkfield Earthquake. *Science*, *318*.

Allmann, B. P., & Shearer, P. M. (2009). Global variations of stress drop for moderate to large earthquakes. *Journal of Geophysical Research: Solid Earth*, *114*.

Ampuero, J.-P., & Ben-Zion, Y. (2008). Cracks, pulses and macroscopic asymmetry of dynamic rupture on a bimaterial interface with velocity-weakening friction. *Geophysical Journal International*, *173*.

Ampuero, J.-P., & Rubin, A. M. (2008). Earthquake nucleation on rate and state faults – Aging and slip laws. *Journal of Geophysical Research: Solid Earth*, *113*.

Andrews, D. J. (1976). Rupture velocity of plane strain shear cracks. *Journal of Geophysical Research*, *81*.

Bakun, W. H., Aagaard, B., Dost, B., Ellsworth, W., Hardebeck, J., Harris, R., … Waldhauser, F. (2005). Implications for Prediction and Hazard Assessment from the 2004 Parkfield Earthquake. *Nature*, *437*.

Bakun, W. H., & Lindh, A. G. (1985). The Parkfield, California, Earthquake Prediction Experiment. *Science*, *229*.

Bakun, W. H., & McEvilly, T. V. (1984). Recurrence models and Parkfield, California, earthquakes. *Journal of Geophysical Research: Solid Earth*, *89*.

Bao, H., Ampuero, J. P., Meng, L., Fielding, E., Liang, C., Milliner, C., … Huang, H. (2019). Early and persistent supershear rupture of the 2018 magnitude 7.5 Palu earthquake. *Nature Geoscience*, *12*.

Barbot, S., Lapusta, N., & Avouac, J.-P. (2012). Under the Hood of the Earthquake Machine: Toward Predictive Modeling of the Seismic Cycle. *Science*, *336*.

Barras, F., Thøgersen, K., Aharonov, E., & Renard, F. (2023). How Do Earthquakes Stop? Insights From a Minimal Model of Frictional Rupture. *Journal of Geophysical Research: Solid Earth*, *128*.

Beeler, N. M., Tullis, T. E., & Goldsby, D. L. (2008). Constitutive relationships and physical basis of fault strength due to flash heating. *Journal of Geophysical Research: Solid Earth*, *113*.

Bilham, R. (2005). Coseismic Strain and the Transition to Surface Afterslip Recorded by Creepmeters near the 2004 Parkfield Epicenter. *Seismological*

Research Letters, *76*.

Blanpied, M. L., Lockner, D. A., & Byerlee, J. D. (1991). Fault stability inferred from granite sliding experiments at hydrothermal conditions. *Geophysical Research Letters*, *18*.

Brengman, C. M. J., Barnhart, W. D., Mankin, E. H., & Miller, C. N. (2019). Earthquake-Scaling Relationships from Geodetically Derived Slip Distributions. *Bulletin of the Seismological Society of America*, *109*.

Bruhat, L., Barbot, S., & Avouac, J.-P. (2011). Evidence for postseismic deformation of the lower crust following the 2004 Mw6.0 Parkfield earthquake. *Journal of Geophysical Research: Solid Earth*, *116*.

Brune, J. N. (1970). Tectonic stress and the spectra of seismic shear waves from earthquakes. *Journal of Geophysical Research*, *75*.

Burridge, R., Conn, G., & Freund, L. B. (1979). The stability of a rapid mode II shear crack with finite cohesive traction. *Journal of Geophysical Research: Solid Earth*, *84*.

Byerlee, J. D. (1978). Friction of rocks. *Pure and Applied Geophysics*, *116*.

California Geological Survey. (1972). *California strong motion instrumentation program.* International Federation of Digital Seismograph Networks. doi: 10.7914/B34Q-BB70

Cattania, C., Hainzl, S., Wang, L., Enescu, B., & Roth, F. (2015). Aftershock triggering by postseismic stresses: A study based on Coulomb rate-and-state models. *Journal of Geophysical Research: Solid Earth*, *120*.

Chang, S.-H., Avouac, J.-P., Barbot, S., & Lee, J.-C. (2013). Spatially variable fault friction derived from dynamic modeling of aseismic afterslip due to the 2004 Parkfield earthquake. *Journal of Geophysical Research: Solid Earth*, *118*.

Churchill, R. M., Werner, M. J., Biggs, J., & Fagereng, Å. (2022). Relative Afterslip Moment Does Not Correlate With Aftershock Productivity: Implications for the Relationship Between Afterslip and Aftershocks. *Geophysical Research Letters*, *49*.

Churchill, R. M., Werner, M. J., Biggs, J., & Fagereng, r. (2024). Spatial Relationships Between Coseismic Slip, Aseismic Afterslip, and On-Fault Aftershock Density in Continental Earthquakes. *Journal of Geophysical Research: Solid Earth*, *129*.

Cocco, M., Aretusini, S., Cornelio, C., Nielsen, S. B., Spagnuolo, E., Tinti, E., & Di Toro, G. (2023). Fracture Energy and Breakdown Work During Earthquakes. *Annual Review of Earth and Planetary Sciences*, *51*.

Cotton, F., & Coutant, O. (1997). Dynamic stress variations due to shear faults in a plane-layered medium. *Geophysical Journal International*, *128*.

Custódio, S., Liu, P., & Archuleta, R. J. (2005). The 2004 Mw6.0 Parkfield, California, earthquake: Inversion of near-source ground motion using multiple data sets. *Geophysical Research Letters*, *32*.

Custódio, S., Page, M. T., & Archuleta, R. J. (2009). Constraining earthquake source inversions with GPS data: 2. A two-step approach to combine seismic and geodetic data sets. *Journal of Geophysical Research: Solid Earth*, *114*.

Dalguer, L. A., & Day, S. M. (2007). Staggered-grid split-node method for spontaneous rupture simulation. *Journal of Geophysical Research: Solid Earth*, *112*.

Das, S. (2015). Supershear Earthquake Ruptures – Theory, Methods, Laboratory Experiments and Fault Superhighways: An Update. *Geotechnical, Geological and Earthquake Engineering*, *39*.

Day, S. M., Dalguer, L. A., Lapusta, N., & Liu, Y. (2005). Comparison of finite difference and boundary integral solutions to three-dimensional spontaneous rupture. *Journal of Geophysical Research: Solid Earth*, *110*.

Dieterich, J. H. (1992). Earthquake nucleation on faults with rate-and state-dependent strength. *Tectonophysics*, *211*.

Dunham, E. M., Belanger, D., Cong, L., & Kozdon, J. E. (2011). Earthquake Ruptures with Strongly Rate-Weakening Friction and Off-Fault Plasticity, Part 1: Planar Faults. *Bulletin of the Seismological Society of America*, *101*.

Fletcher, J. B., Spudich, P., & Baker, L. M. (2006). Rupture Propagation of the 2004 Parkfield, California, Earthquake from Observations at the UPSAR. *Bulletin of the Seismological Society of America*, *96*.

Freed, A. M. (2007). Afterslip (and only afterslip) following the 2004 Parkfield, California, earthquake. *Geophysical Research Letters*, *34*.

Freund, L. B. (1979). The mechanics of dynamic shear crack propagation. *Journal of Geophysical Research: Solid Earth*, *84*.

Fukuyama, E., & Mikumo, T. (1993). Dynamic rupture analysis: Inversion for the source process of the 1990 Izu-Oshima, Japan, earthquake (M = 6.5). *Journal* *of Geophysical Research: Solid Earth*, *98*.

Gabriel, A.-A., Ampuero, J.-P., Dalguer, L. A., & Mai, P. M. (2012). The transition of dynamic rupture styles in elastic media under velocity-weakening friction. *Journal of Geophysical Research: Solid Earth*, *117*.

Gabriel, A.-A., Ampuero, J.-P., Dalguer, L. A., & Mai, P. M. (2013). Source properties of dynamic rupture pulses with off-fault plasticity. *Journal of Geophysical Research: Solid Earth*, *118*.

Gabriel, A.-A., Garagash, D. I., Palgunadi, K. H., & Mai, P. M. (2023). *Fault-size dependent fracture energy explains multi-scale seismicity and cascading earthquakes.*

Gallovič, F., Valentová, L., Ampuero, J.-P., & Gabriel, A.-A. (2019a). Bayesian Dynamic Finite-Fault Inversion: 1. Method and Synthetic Test. *Journal of Geophysical Research: Solid Earth*, *124*.

Gallovič, F., Valentová, L., Ampuero, J.-P., & Gabriel, A.-A. (2019b). Bayesian Dynamic Finite-Fault Inversion: 2. Application to the 2016 Mw 6.2 Amatrice, Italy, Earthquake. *Journal of Geophysical Research: Solid Earth*, *124*.

Gallovič, F., Zahradník, J., Plicka, V., Sokos, E., Evangelidis, C., Fountoulakis, I., & Turhan, F. (2020). Complex rupture dynamics on an immature fault during the 2020 Mw 6.8 Elazığ earthquake, Turkey. *Commun. Earth Environ.*, *1*.

Gallovič, F. (2008). Heterogeneous Coulomb stress perturbation during earthquake cycles in a 3D rate-and-state fault model. *Geophysical Research Letters*, *35*.

Harris, R. A., Barall, M., Aagaard, B., Ma, S., Roten, D., Olsen, K., … Dalguer, L. (2018). A Suite of Exercises for Verifying Dynamic Earthquake Rupture Codes. *Seismological Research Letters*, *89*.

Heaton, T. H. (1990). Evidence for and implications of self-healing pulses of slip in earthquake rupture. *Physics of the Earth and Planetary Interiors*, *64*.

Heinecke, A., Breuer, A., Rettenberger, S., Bader, M., Gabriel, A.-A., Pelties, C., … Dubey, P. (2014). Petascale High Order Dynamic Rupture Earthquake Simulations on Heterogeneous Supercomputers. In *SC '14: Proceedings of the International Conference for High Performance Computing, Networking, Storage and Analysis.*

Hickman, S., & Zoback, M. (2004). Stress orientations and magnitudes in the SAFOD pilot hole. *Geophysical Research Letters*, *31*.

Jiang, J., Bock, Y., & Klein, E. (2021a). Coevolving early afterslip and aftershock signatures of a San Andreas fault rupture. *Science Advances*, *7*.

Jiang, J., Bock, Y., & Klein, E. (2021b). *Data and Models for 'Coevolving Early Afterslip and Aftershock Signatures of a San Andreas Fault Rupture'* [data set]. Zenodo. doi: 10.5281/zenodo.4278477

Johanson, I. A., Fielding, E. J., Rolandone, F., & Bürgmann, R. (2006). Coseismic and Postseismic Slip of the 2004 Parkfield Earthquake from Space-Geodetic Data. *Bulletin of the Seismological Society of America*, *96*.

Johnson, K. M., Bürgmann, R., & Larson, K. (2006). Frictional Properties on the San Andreas Fault near Parkfield, California, Inferred from Models of Afterslip following the 2004 Earthquake. *Bulletin of the Seismological Society of America*, *96*.

Kagan, Y. Y., & Houston, H. (2005). Relation between mainshock rupture process and Omori's law for aftershock moment release rate. *Geophysical Journal International*, *163*.

Kaneko, Y., & Shearer, P. M. (2014). Seismic source spectra and estimated stress drop derived from cohesive-zone models of circular subshear rupture. *Geophysical Journal International*, *197*.

Ke, C.-Y., McLaskey, G. C., & Kammer, D. S. (2018). Rupture Termination in Laboratory-Generated Earthquakes. *Geophysical Research Letters*, *45*.

Kim, A., & Dreger, D. S. (2008). Rupture process of the 2004 Parkfield earthquake from near-fault seismic waveform and geodetic records. *Journal of Geophysical Research: Solid Earth*, *113*.

Kostka, F., & Gallovič, F. (2016). Static Coulomb stress load on a three-dimensional rate-and-state fault: Possible explanation of the anomalous delay of the 2004 Parkfield earthquake. *Journal of Geophysical Research: Solid Earth*, *121*.

Krenz, L., Uphoff, C., Ulrich, T., Gabriel, A.-A., Abrahams, L. S., Dunham, E. M., & Bader, M. (2021). 3D acoustic-elastic coupling with gravity: the dynamics of the 2018 Palu, Sulawesi earthquake and tsunami. In *Proceedings of the international conference for high performance computing, networking, storage and analysis.* Association for Computing Machinery.

Lachenbruch, A. H., & Sass, J. H. (1980). Heat flow and energetics of the San Andreas Fault Zone. *Journal of Geophysical Research: Solid Earth*, *85*.

Lambert, V., Lapusta, N., & Perry, S. (2021). Propagation of large earthquakes as self-healing pulses or mild cracks. *Nature*, *591*.

Langbein, J., Borcherdt, R., Dreger, D., Fletcher, J., Hardebeck, J. L., Hellweg, M., … Treiman, J. A. (2005). Preliminary Report on the 28 September 2004, M 6.0 Parkfield, California Earthquake. *Seismological Research Letters*, *76*.

Langbein, J., Murray, J. R., & Snyder, H. A. (2006). Coseismic and Initial Post-seismic Deformation from the 2004 Parkfield, California, Earthquake, Observed by Global Positioning System, Electronic Distance Meter, Creepmeters, and Borehole Strainmeters. *Bulletin of the Seismological Society of America*, *96*.

Lapusta, N., Rice, J. R., Ben-Zion, Y., & Zheng, G. (2000). Elastodynamic analysis for slow tectonic loading with spontaneous rupture episodes on faults with rate- and state-dependent friction. *Journal of Geophysical Research: Solid Earth*, *105*.

Lewis, M. A., & Ben-Zion, Y. (2010). Diversity of fault zone damage and trapping structures in the Parkfield section of the San Andreas Fault from comprehensive analysis of near fault seismograms. *Geophysical Journal International*, *183*.

Li, Y.-G., Leary, P., Aki, K., & Malin, P. (1990). Seismic Trapped Modes in the Oroville and San Andreas Fault Zones. *Science*.

Lienkaemper, J. J., Baker, B., & McFarland, F. S. (2006). Surface Slip Associated with the 2004 Parkfield, California, Earthquake Measured on Alinement Arrays. *Bulletin of the Seismological Society of America*, *96*.

Lisowski, M., Savage, J. C., & Prescott, W. H. (1991). The velocity field along the San Andreas Fault in central and southern California. *Journal of Geophysical Research: Solid Earth*, *96*.

Liu, P., Custódio, S., & Archuleta, R. J. (2006). Kinematic Inversion of the 2004 M 6.0 Parkfield Earthquake Including an Approximation to Site Effects. *Bulletin of the Seismological Society of America*, *96*.

Lockner, D., Morrow, C., Moore, D., & Hickman, S. (2011). Low strength of deep San Andreas Fault gouge from SAFOD core. *Nature*, *472*.

Lui, S. K. Y., & Lapusta, N. (2018). Modeling High Stress Drops, Scaling, Interaction, and Irregularity of Repeating Earthquake Sequences Near Parkfield. *Journal of Geophysical Research: Solid Earth*, *123*.

Ma, S., Custódio, S., Archuleta, R. J., & Liu, P. (2008). Dynamic modeling of the 2004 Mw 6.0 Parkfield, California, earthquake. *Journal of Geophysical Research: Solid Earth*, *113*.

Madariaga, R. (1976). Dynamics of an expanding circular fault. *Bulletin of the Seismological Society of America*, *66*.

Madariaga, R. (1977). High-frequency radiation from crack (stress drop) models of earthquake faulting. *Geophysical Journal International*, *51*.

Madden, E. H., Ulrich, T., & Gabriel, A.-A. (2022). The State of Pore Fluid Pressure and 3-D Megathrust Earthquake Dynamics. *Journal of Geophysical Research: Solid Earth*, *127*.

Metropolis, N., Rosenbluth, A. W., Rosenbluth, M. N., Teller, A. H., & Teller, E. (1953). Equation of State Calculations by Fast Computing Machines. *The Journal of Chemical Physics*, *21*.

Mikumo, T., & Miyatake, T. (1995). Heterogeneous distribution of dynamic stress drop and relative fault strength recovered from the results of waveform inversion: the 1984 Morgan Hill, California, earthquake. *Bulletin of the Seismological Society of America*, *85*.

Murray, J., & Langbein, J. (2006). Slip on the San Andreas Fault at Parkfield, California, over Two Earthquake Cycles, and the Implications for Seismic Hazard. *Bulletin of the Seismological Society of America*, *96*.

Neves, M., Peng, Z., & Lin, G. (2022). A High-Resolution Earthquake Catalog for the 2004 Mw 6 Parkfield Earthquake Sequence Using a Matched Filter Technique. *Seismological Research Letters*, *94*.

Noda, H., Dunham, E. M., & Rice, J. R. (2009). Earthquake ruptures with thermal weakening and the operation of major faults at low overall stress levels. *Journal of Geophysical Research: Solid Earth*, *114*.

Noda, H., & Lapusta, N. (2010). 3D simulations of long-term fault slip with dynamic weakening: relation between locked patches and earthquake-induced stress changes. In *Workshop on earthquake source dynamics: Data and data-constrained numerical modeling.*

Oeser, J., Bunge, H.-P., & Mohr, M. (2006). Cluster design in the earth sciences tethys. In M. Gerndt & D. Kranzlmüller (Eds.), *High performance computing and communications.* Springer Berlin Heidelberg.

Okada, Y. (1985). Surface deformation due to shear and tensile faults in a half-space. *Bulletin of the Seismological Society of America*, *75*.

Olsen, K. B., Day, S. M., & Bradley, C. R. (2003). Estimation of Q for Long-Period (>2 sec) Waves in the Los Angeles Basin. *Bulletin of the Seismological Society of America*, *93*.

Page, M. T., Custódio, S., Archuleta, R. J., & Carlson, J. M. (2009). Constraining earthquake source inversions with GPS data: 1. Resolution-based removal of artifacts. *Journal of Geophysical Research: Solid Earth*, *114*.

Palgunadi, K. H., Gabriel, A.-A., Garagash, D. I., Ulrich, T., & Mai, P. M. (2024). Rupture Dynamics of Cascading Earthquakes in a Multiscale Fracture Network. *Journal of Geophysical Research: Solid Earth*, *129*.

Peng, Z., & Zhao, P. (2009). Migration of early aftershocks following the 2004 Parkfield earthquake. *Nature Geoscience*, *2*.

Peyrat, S., & Olsen, K. B. (2004). Nonlinear dynamic rupture inversion of the 2000 Western Tottori, Japan, earthquake. *Geophysical Research Letters*, *31*.

Premus, J., Gallovič, F., & Ampuero, J.-P. (2022). Bridging time scales of faulting: From coseismic to postseismic slip of the M_w 6.0 2014 South Napa, California earthquake. *Science Advances*, *8*.

Premus, J., Gallovič, F., Hanyk, L., & Gabriel, A. (2020). FD3D_TSN: A Fast and Simple Code for Dynamic Rupture Simulations with GPU Acceleration. *Seismological Research Letters*, *91*.

Press, F. (1968). Earth models obtained by Monte Carlo Inversion. *Journal of Geophysical Research (1896-1977)*, *73*.

Pulido, N., & Dalguer, L. A. (2009). Estimation of the High-Frequency Radiation of the 2000 Tottori (Japan) Earthquake Based on a Dynamic Model of Fault Rupture: Application to the Strong Ground Motion Simulation. *Bulletin of the Seismological Society of America*, *99*.

Quin, H. (1990). Dynamic stress drop and rupture dynamics of the October 15, 1979 Imperial Valley, California, earthquake. *Tectonophysics*, *175*.

Rekoske, J. M., Gabriel, A.-A., & May, D. A. (2023). Instantaneous Physics-Based Ground Motion Maps Using Reduced-Order Modeling. *Journal of Geophysical Research: Solid Earth*, *128*.

Rice, J. R. (1992). Fault Stress States, Pore Pressure Distributions, and the Weakness of the San Andreas Fault. In B. Evans & T. fong Wong (Eds.), *Fault mechanics and transport properties of rocks* (Vol. 51, p. 475-503). Academic Press.

Rice, J. R. (1993). Spatio-temporal complexity of slip on a fault. *Journal of Geophysical Research: Solid Earth*, *98*.

Rice, J. R. (2006). Heating and weakening of faults during earthquake slip. *Journal of Geophysical Research: Solid Earth*, *111*.

Rice, J. R., & Ben-Zion, Y. (1996). Slip complexity in earthquake fault models. *Proceedings of the National Academy of Sciences*, *93*.

Rucker, C., & Erickson, B. A. (2023). *Physics-Informed Deep Learning of Rate-and-State Fault Friction.*

Ruina, A. (1983). Slip instability and state variable friction laws. *Journal of Geophysical Research: Solid Earth*, *88*.

Rymer, M. J., Tinsley, I., John C., Treiman, J. A., Arrowsmith, J. R., Clahan, K. B., Rosinski, A. M., ... Bawden, G. W. (2006). Surface Fault Slip Associated with the 2004 Parkfield, California, Earthquake. *Bulletin of the Seismological Society of America*, *96*.

Sambridge, M. (2013). A Parallel Tempering algorithm for probabilistic sampling and multimodal optimization. *Geophysical Journal International*, *196*.

Schliwa, N. (2024). *FD3D_TSN/2004Parkfield* [software]. Zenodo. doi: 10.5281/zenodo.11072717

Schliwa, N., & Gabriel, A. (2023). Equivalent Near-Field Corner Frequency Analysis of 3D Dynamic Rupture Simulations Reveals Dynamic Source Effects. *Seismological Research Letters*.

Schmedes, J., Archuleta, R. J., & Lavallée, D. (2010). Correlation of earthquake source parameters inferred from dynamic rupture simulations. *Journal of Geophysical Research: Solid Earth*, *115*.

Shi, Z., & Day, S. M. (2013). Rupture dynamics and ground motion from 3-D rough-fault simulations. *Journal of Geophysical Research: Solid Earth*, *118*.

Simpson, R. W., Barall, M., Langbein, J., Murray, J. R., & Rymer, M. J. (2006). San Andreas Fault Geometry in the Parkfield, California, Region. *Bulletin of the Seismological Society of America*, *96*.

Sokal, A. (1997). Monte carlo methods in statistical mechanics: Foundations and new algorithms. In *Functional integration: Basics and applications.* Springer US.

Stiernström, V., Almquist, M., & Dunham, E. M. (2024). *Adjoint-based inversion for stress and frictional parameters in earthquake modeling.*

Suppe, J. (2014). Fluid overpressures and strength of the sedimentary upper crust. *Journal of Structural Geology*, *69*.

Tarantola, A. (2005). *Inverse Problem Theory and Methods for Model Parameter Estimation.* SIAM.

Taufiqurrahman, T., Gabriel, A.-A., Li, D., Ulrich, T., Li, B., Carena, S., ... Gallovič, F. (2023). Dynamics, interactions and delays of the 2019 Ridgecrest rupture sequence. *Nature*.

Thurber, C., Zhang, H., Waldhauser, F., Hardebeck, J., Michael, A., & Eberhart-Phillips, D. (2006). Three-Dimensional Compressional Wavespeed Model, Earthquake Relocations, and Focal Mechanisms for the Parkfield, California, Region. *Bulletin of the Seismological Society of America*, *96*.

Tinti, E., Casarotti, E., Ulrich, T., Taufiqurrahman, T., Li, D., & Gabriel, A.-A. (2021). Constraining families of dynamic models using geological, geodetic and strong ground motion data: The Mw 6.5, October 30th, 2016, Norcia earthquake, Italy. *Earth and Planetary Science Letters*, *576*.

Titus, S. J., DeMets, C., & Tikoff, B. (2005). New slip rate estimates for the creeping segment of the San Andreas fault, California. *Geology*, *33*.

Tong, X., Sandwell, D. T., & Smith-Konter, B. (2013). High-resolution interseismic velocity data along the San Andreas Fault from GPS and InSAR. *Journal of Geophysical Research: Solid Earth*, *118*.

Twardzik, C., Das, S., & Madariaga, R. (2014). Inversion for the physical parameters that control the source dynamics of the 2004 Parkfield earthquake. *Journal of Geophysical Research: Solid Earth*, *119*.

Twardzik, C., Madariaga, R., Das, S., & Custódio, S. (2012). Robust features of the source process for the 2004 Parkfield, California, earthquake from strong-motion seismograms. *Geophysical Journal International*, *191*.

Ulrich, T., Gabriel, A.-A., Ampuero, J.-P., & Xu, W. (2019). Dynamic viability of the 2016 Mw 7.8 Kaikōura earthquake cascade on weak crustal faults. *Nature Communications*.

Uphoff, C., Rettenberger, S., Bader, M., Madden, E. H., Ulrich, T., Wollherr, S., & Gabriel, A.-A. (2017). Extreme scale multi-physics simulations of the tsunamigenic 2004 sumatra megathrust earthquake. In *Proceedings of the international conference for high performance computing, networking, storage and analysis.* Association for Computing Machinery.

Utsu, T., Ogata, Y., S, R., & Matsu'ura. (1995). The Centenary of the Omori Formula for a Decay Law of Aftershock Activity. *Journal of Physics of the Earth*, *43*.

Vavra, E., Fialko, Y., Rockwell, T. K., Bilham, R., Stepancikova, P., Stemberk, J., ... Stemberk, J. (2023). Characteristic Slow-Slip Events on the Superstition Hills Fault, Southern California. *ESS Open Archive*.

Wen, Y., Cai, J., He, K., & Xu, C. (2024). Dynamic Rupture of the 2021 MW 7.4 Maduo Earthquake: An Intra-Block Event Controlled by Fault Geometry. *Journal of Geophysical Research: Solid Earth*, *129*.

Williams, C. F., Grubb, F. V., & Galanis Jr., S. P. (2004). Heat flow in the SAFOD pilot hole and implications for the strength of the San Andreas Fault. *Geophysical Research Letters*, *31*.

Supporting Information for "The linked complexity of coseismic and postseismic faulting revealed by seismo-geodetic dynamic inversion of the 2004 Parkfield earthquake"

Nico Schliwa [1], Alice-Agnes Gabriel [2,1], Jan Premus [3], František Gallovič [4]

[1]Ludwig-Maximilians-Universität München, Munich, Germany

[2]Scripps Institution of Oceanography, UC San Diego, La Jolla, CA, USA

[3]Côte d'Azur University, Nice, France

[4]Charles University, Prague, Czech Republic

Contents of this file

1. Figures S1 to S14
2. Tables S1 to S2

Additional Supporting Information (Files uploaded separately)

1. Captions for Movies S1 to S2

Introduction This document contains supplementary figures, tables, and movie captions to augment the main manuscript.

Movie S1. Coseismic slip rate evolution of the preferred dynamic rupture and afterslip model. The black contour shows the coseismic rupture extent and the star marks the hypocenter.

Movie S2. 90-day postseismic slip rate evolution of the preferred joint dynamic rupture and afterslip model. Light blue dots show aftershocks during the latest 20% of the time since the mainshock and grey dots show the remaining aftershocks since the mainshock. The black line shows the coseismic rupture extent and the star marks the hypocenter.

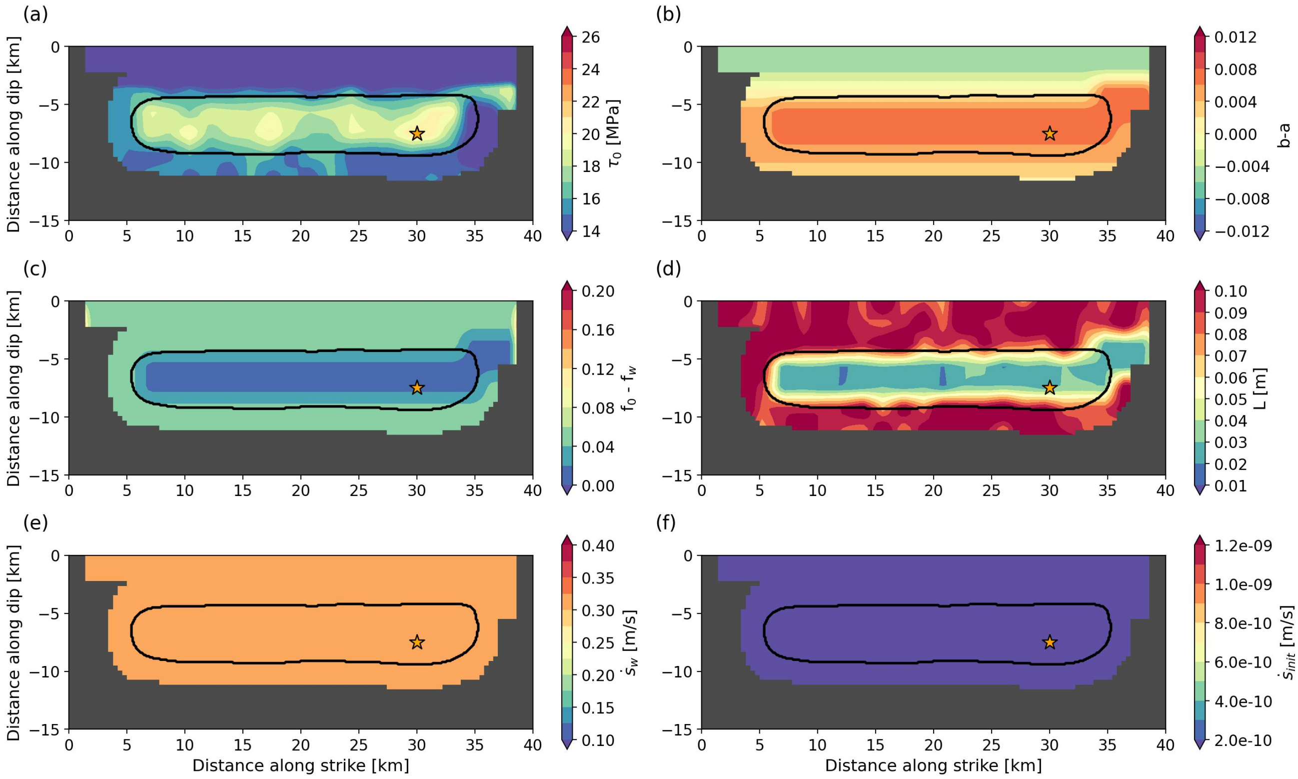

Figure S1. Dynamic parameters of the initial dynamic rupture model based on "Model B" of Ma et al. (2008). The parameters are bilinearly interpolated from the model grid (Fig. 1d) onto the grid of the quasi-dynamic solver, which has a 400 m spacing. We consider parameters to be unconstrained in all areas of the fault where the overall fault slip (coseismic + postseismic) does not exceed 10 cm within a radius of 1.2 km. We do not show dynamic parameters on these unconstrained fault grid points. The black line indicates the extent of the coseismic rupture, and the star marks the hypocenter of the mainshock. (a) Prestress τ_0. (b) Difference between the state evolution and the direct effect parameter, $b-a$. (c) Friction drop $f_0 - f_w$. (d) Characteristic slip distance L. (e) Weakening slip rate $\dot{s}_w$. (f) Initial slip rate $\dot{s}_{init}$.

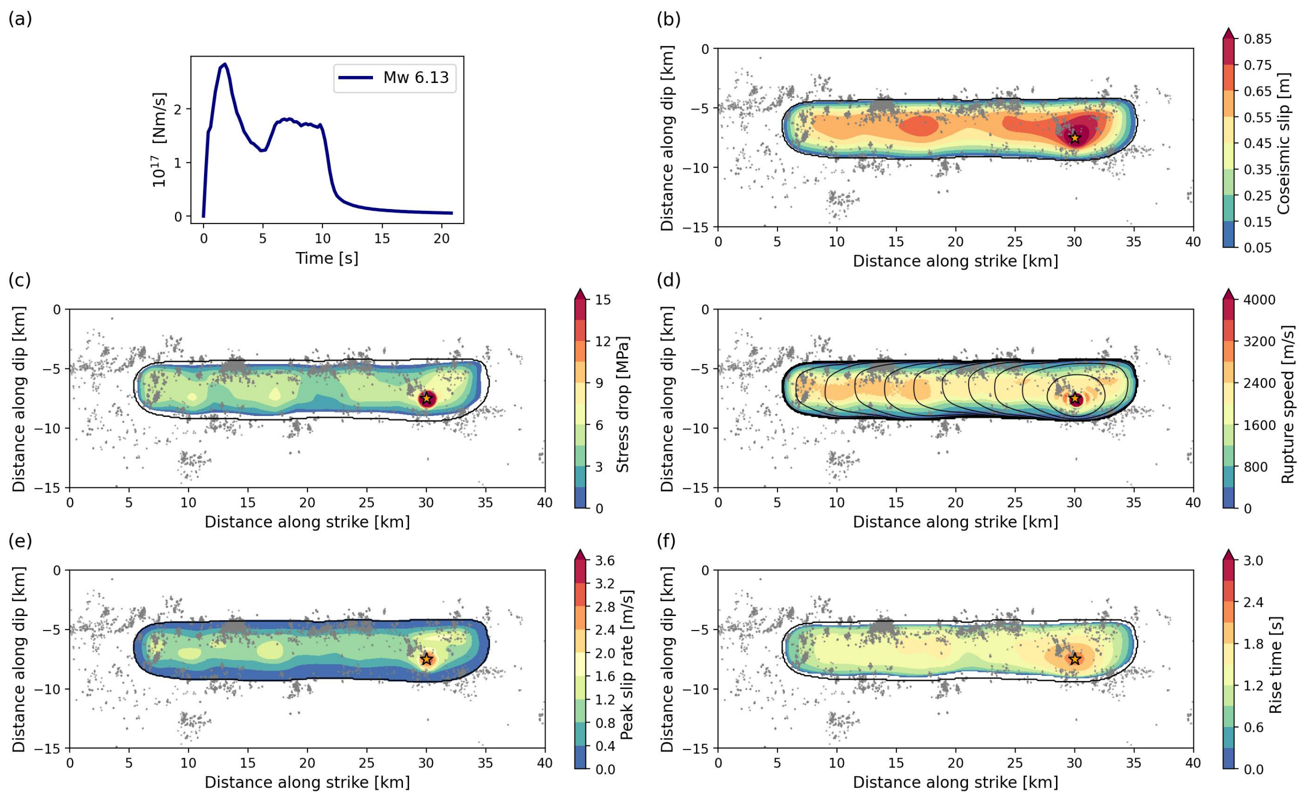

Figure S2. Coseismic dynamic rupture parameters of the initial dynamic rupture model based on "Model B" of Ma et al. (2008). Grey dots show 90-day aftershock locations (Neves et al., 2022) projected on the planar fault plane, the black contour indicates the coseismic rupture extent, and the star marks the hypocenter. (a) Moment release rate and moment magnitude. (b) Coseismic slip. (c) Stress drop. (d) Local rupture speed and rupture front contours every 1 s. (e) Peak slip rate. (f) Rise time.

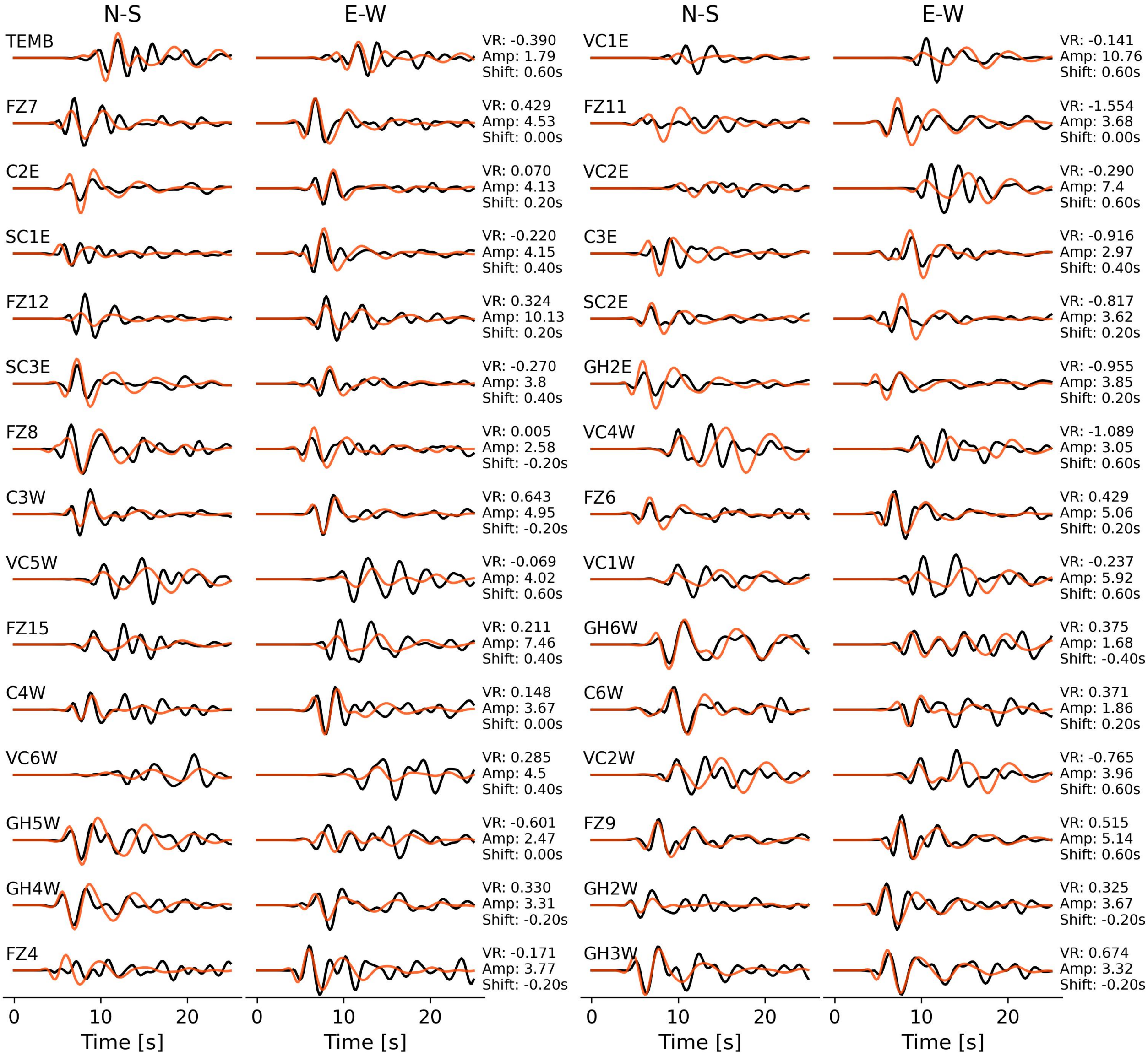

Figure S3. Observed (black) and synthetic (orange) seismic velocity waveforms from the initial dynamic rupture model based on "Model B" of Ma et al. (2008), bandpass filtered between 0.16–0.5 Hz at the 30 stations used to constrain the inversion. Each waveform (synthetic and observed) is normalized by the respective station's maximum amplitude (Amp, in cm/s, either synthetic or observed maximum). The observed waveforms at each station are cross-correlated and time-shifted relative to the synthetics to maximize the variance reduction (VR) and to account for unmodeled effects of topography and the 3D velocity structure.

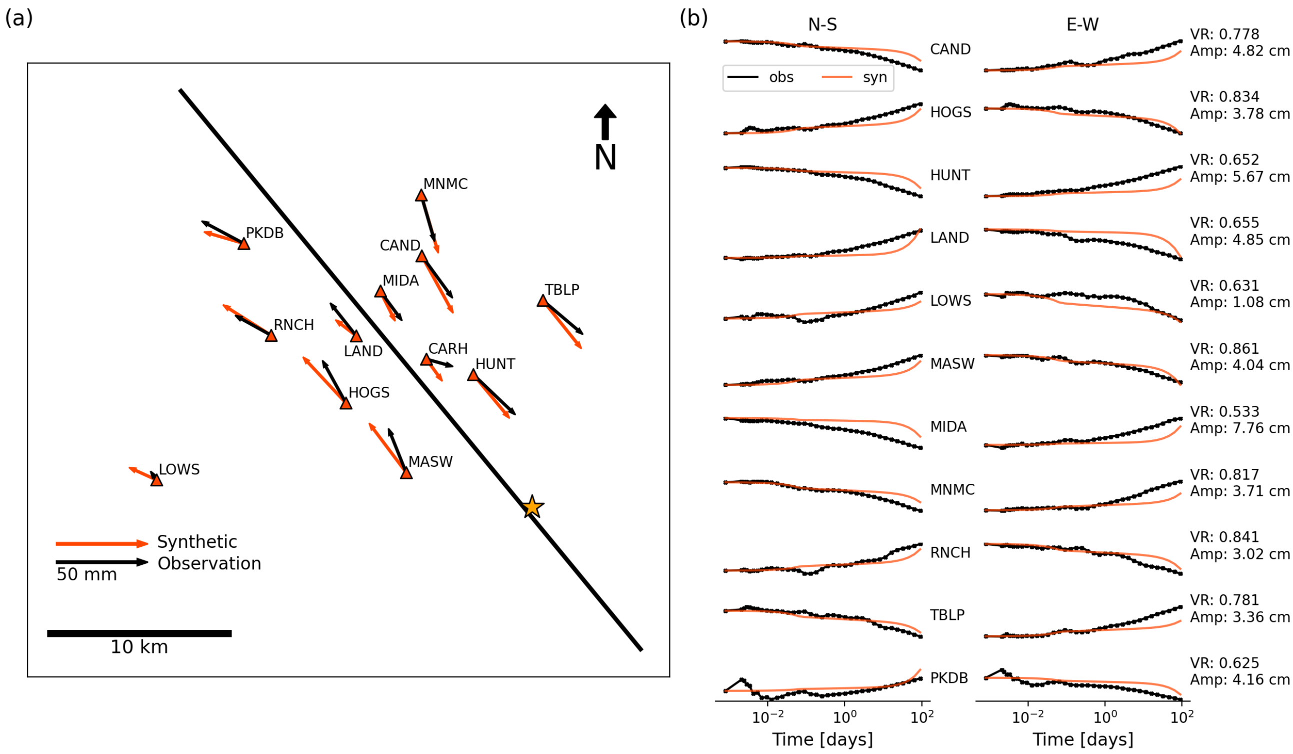

Figure S4. (a) Coseismic horizontal static displacements at 12 GPS stations. Black and orange arrows show observed (Jiang et al., 2021) and synthetic displacements from the initial dynamic rupture model based on "Model B" of Ma et al. (2008), respectively. The black line indicates the fault trace, and the star marks the epicenter. Both synthetic and observed coseismic displacements are given at 90 s after the rupture onset. (b) Postseismic evolution of the normalized displacements at 11 GPS stations (excluding station CARH) during the first 90 days following the earthquake. Black curves show observations (Jiang et al., 2021), and orange curves show the synthetics of our initial model. The time scale is logarithmic. For each station, we annotate its variance reduction inferred after removing the coseismic displacement and its maximum amplitude.

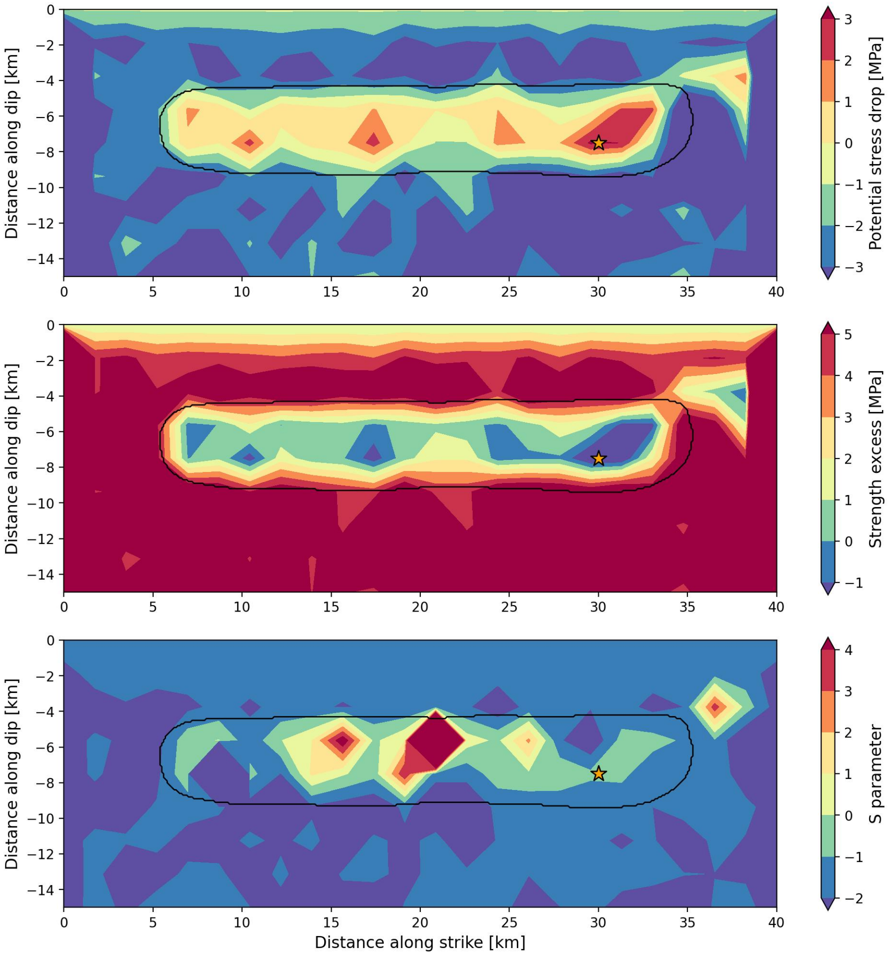

Figure S5. Derived quantities from the dynamic parameters of the initial dynamic rupture model based on "Model B" of Ma et al. (2008). The black contour indicates the coseismic rupture extent, and the star marks the hypocenter. (a) Potential stress drop ($\tau_0 - f_w\sigma_n$). (b) Strength excess ($f_0\sigma_n - \tau_0$). (c) S parameter ($\frac{\tau^y - \tau^0}{\tau^0 - \tau^d}$).

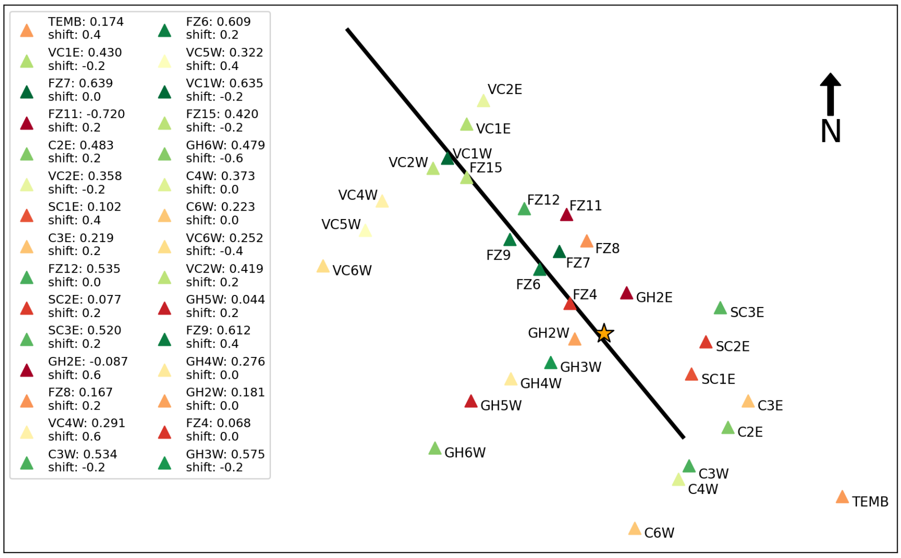

Figure S6. Stations used for constraining the inversion colored by their seismic variance reductions obtained from the preferred joint dynamic rupture and afterslip model. The star marks the epicenter and the black line shows the fault trace of our model's planar fault.

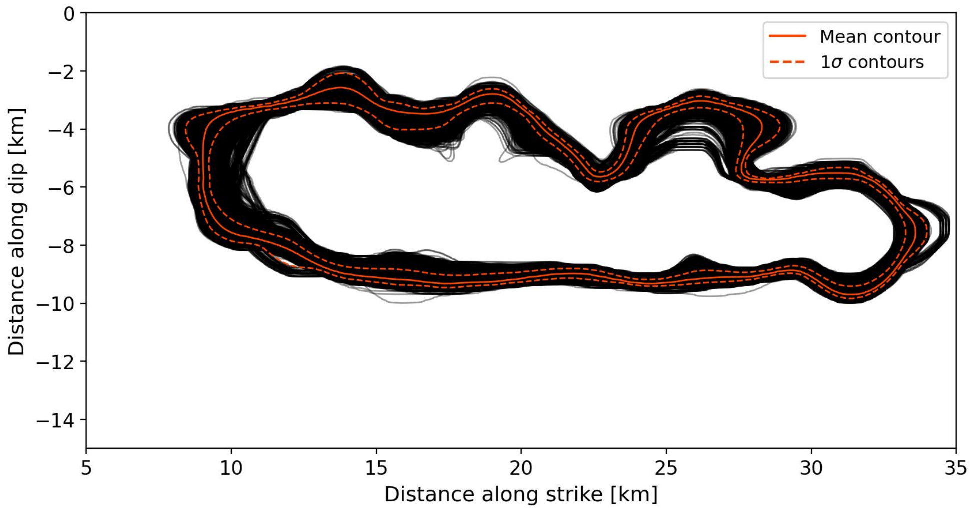

Figure S7. Dynamic rupture extent contours of the 10500 models of the best-fitting ensemble. Orange and dashed orange lines show the mean rupture edge and one standard deviation in both directions, respectively.

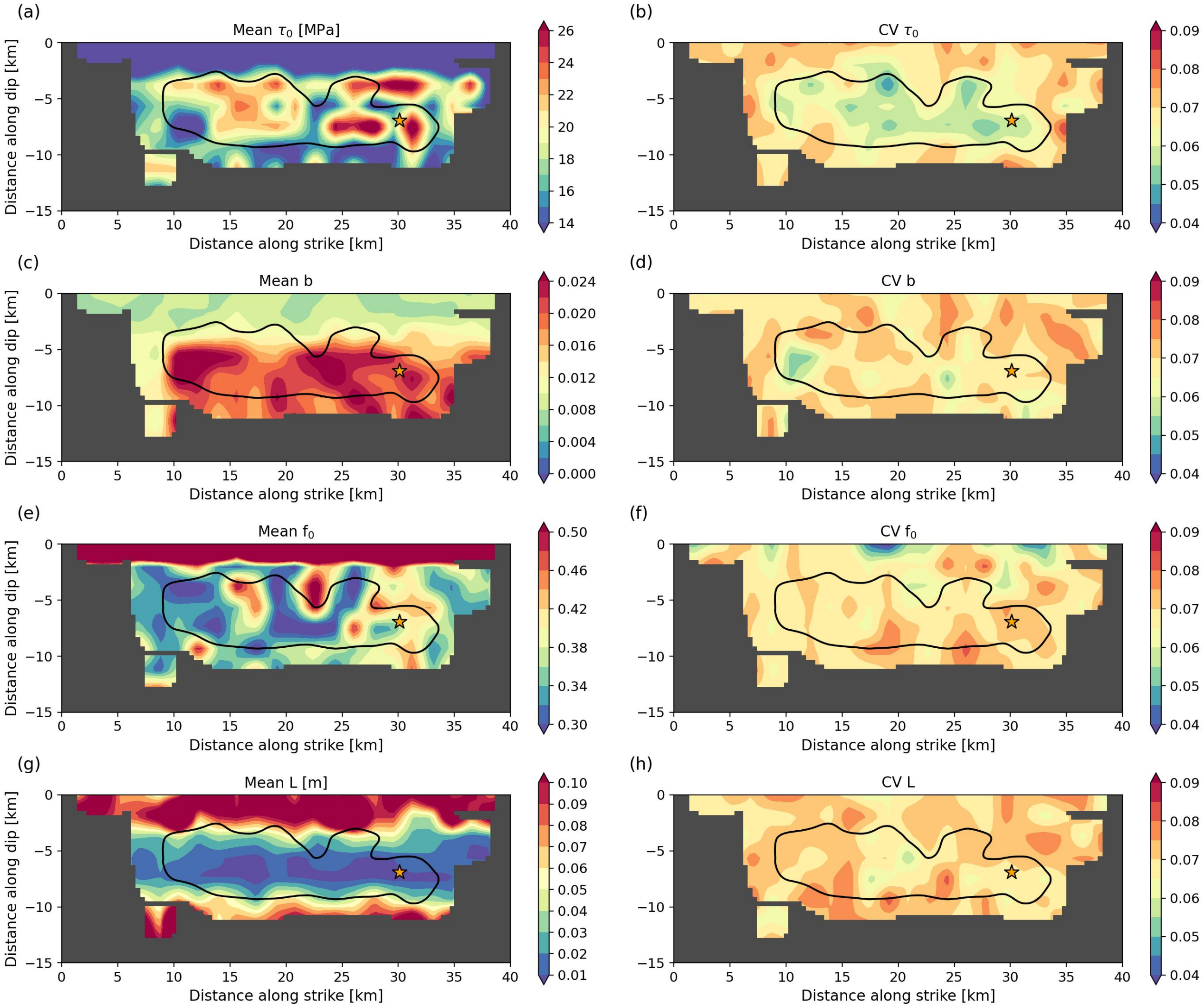

Figure S8. Mean distributions of the best-fitting model ensemble's (a) prestress τ_0, (c) $b-a$, (e) friction drop $f_0 - f_w$, (g) characteristic weakening distance L, and their corresponding coefficients of variation CV (b,d,f,h). The model ensemble contains 10500 models. We mask areas where the sum of coseismic and postseismic slip does not exceed 10 cm within 1.2 km, which we consider unconstrained.

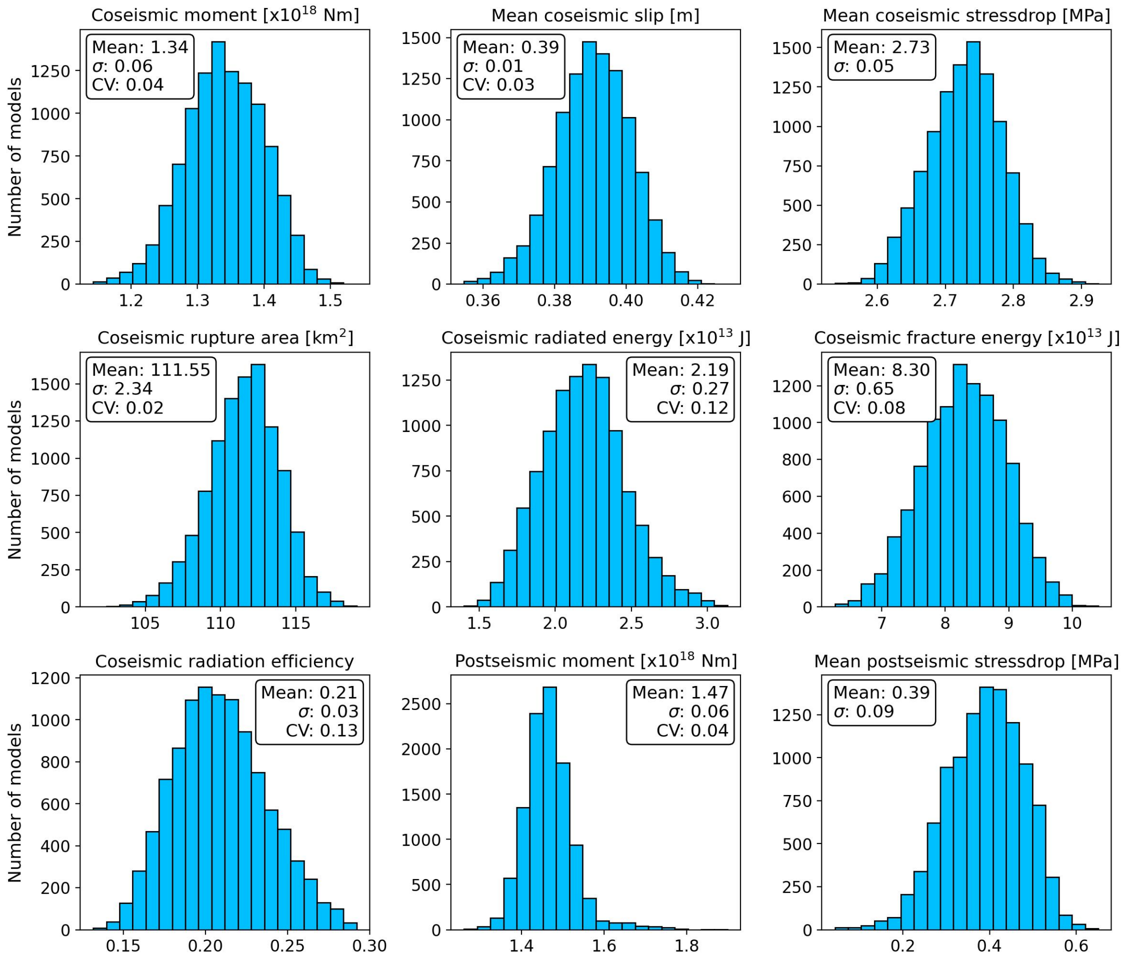

Figure S9. Histograms of various coseismic and postseismic rupture parameters of the best-fitting model ensemble containing 10500 unique joint dynamic rupture and afterslip models. Legends of each subplot show mean values, standard deviations σ, and coefficients of variation CV (ratio of the standard deviation to the mean) for quantities with an absolute zero.

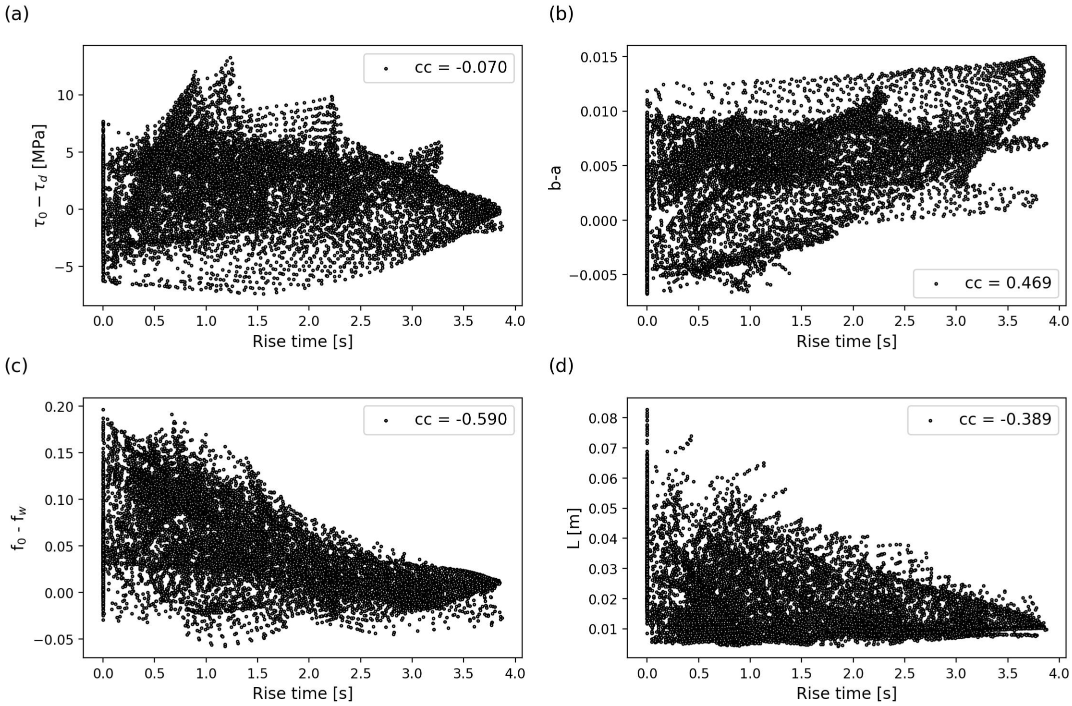

Figure S10. Rise times of each grid point of the preferred joint dynamic rupture and afterslip model plotted against (a) τ_0, (b) $b - a$, (c), $f_0 - f_w$, (d) L. Subplot legends show correlation coefficients between both variables.

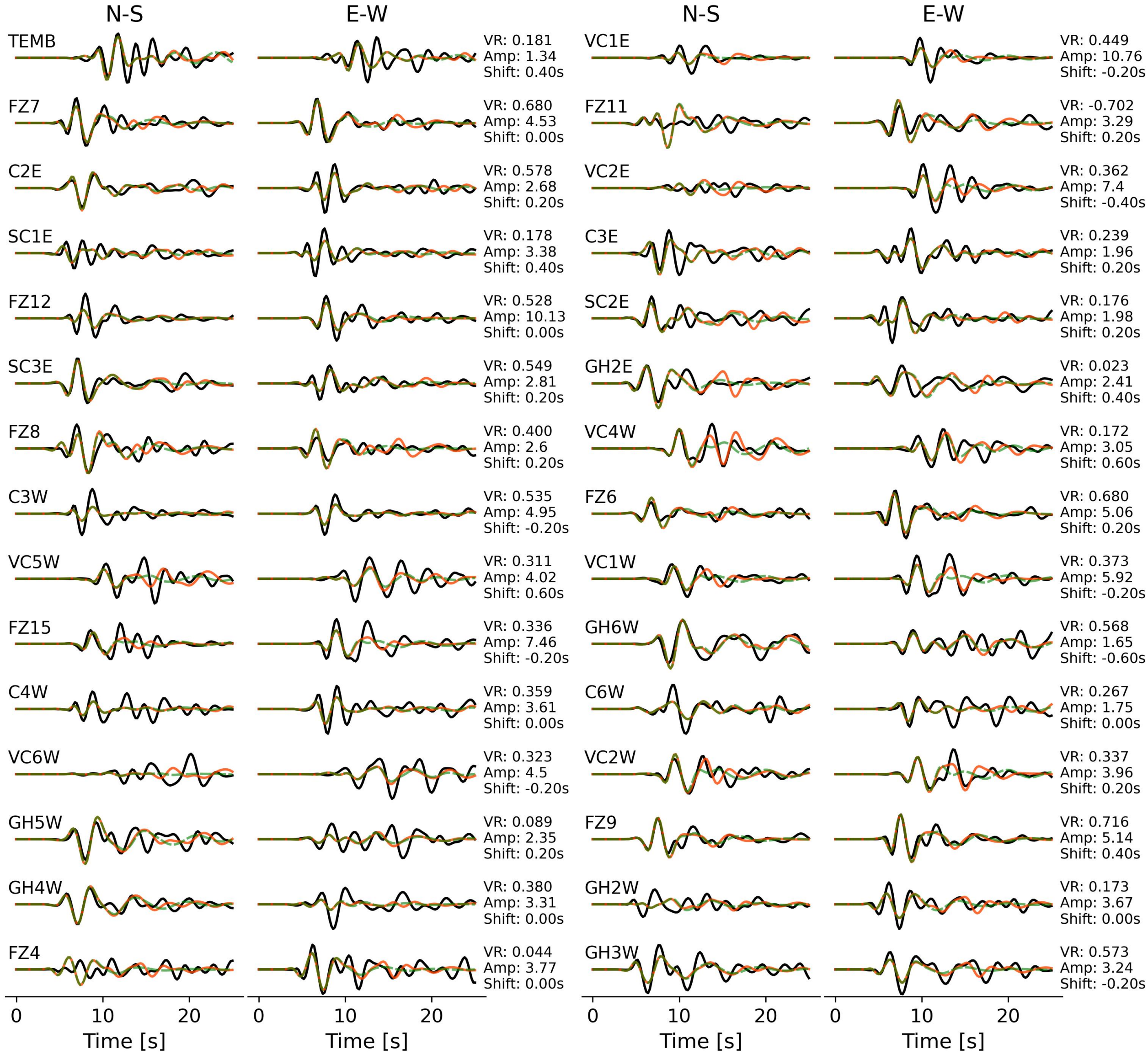

Figure S11. Observed (black) and synthetic (dashed green) velocity waveforms from a **5 s version** of the preferred joint dynamic rupture and afterslip model (including only the initial pulse-like rupture phase) filtered between 0.16 and 0.5 Hz at the 30 stations used to constrain the inversion. The reference model's waveforms (21 s simulation duration) are shown in orange. Each waveform is normalized by the respective station's maximum amplitude (Amp in cm/s). The variance reductions (VR) of the 5 s version are annotated. The observed waveforms at each station are shifted relative to the reference synthetics to account for the effects of topography and the 3D velocity structure by maximizing the VR.

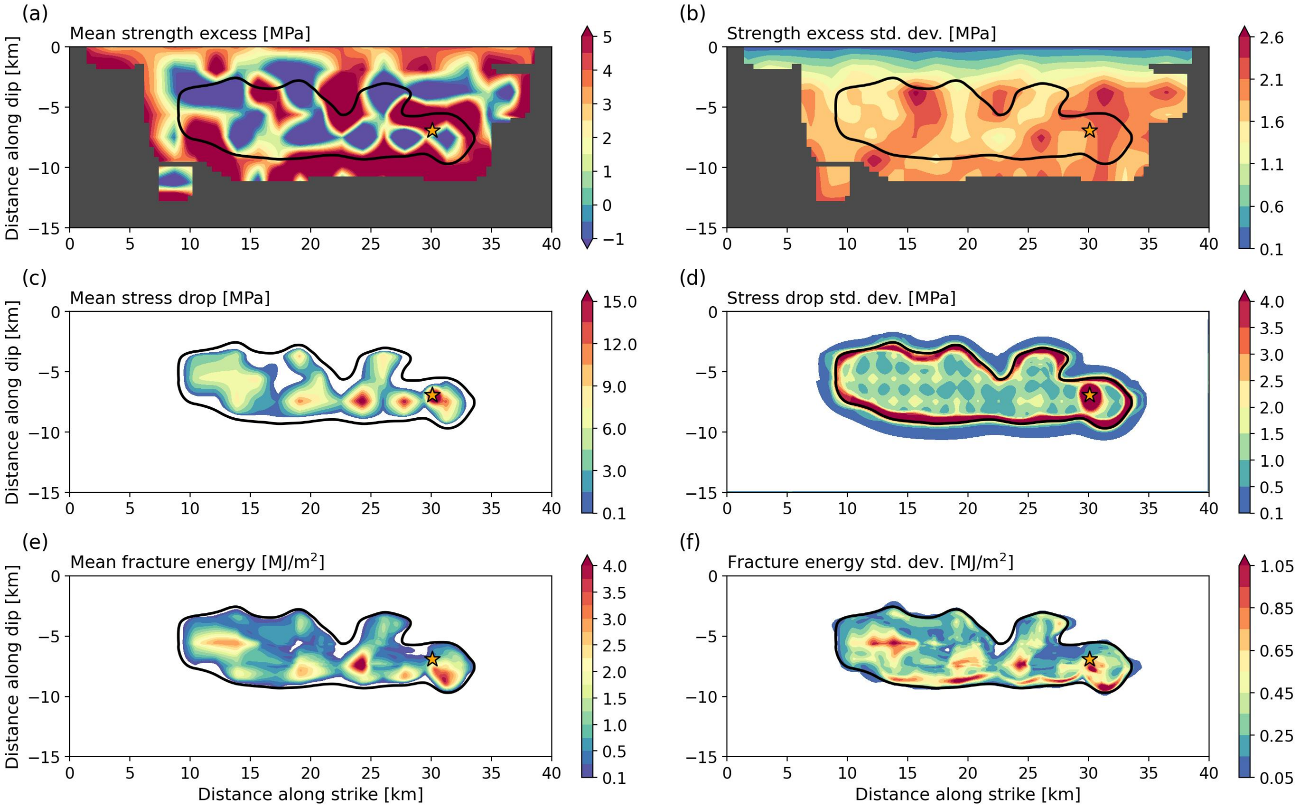

Figure S12. Means of the best-fitting model ensemble's (a) initial strength excess ($f_0\sigma_n - \tau_0$), (c) coseismic stress drop (e) coseismic fracture energy distributions, and the corresponding standard deviations (b,d,f). The model ensemble contains 10500 models. We only show the strength excess where coseismic and postseismic slip combined exceed 10 cm somewhere within a radius of 1.2 km, which we consider as constrained by the inversion.

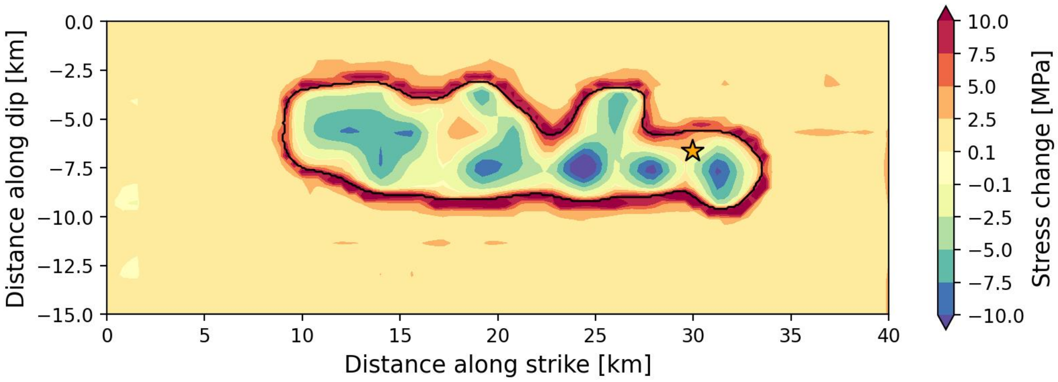

Figure S13. Coseismic stress change of the preferred joint dynamic rupture and afterslip model. The black line indicates the coseismic rupture extent and the star marks the hypocenter.

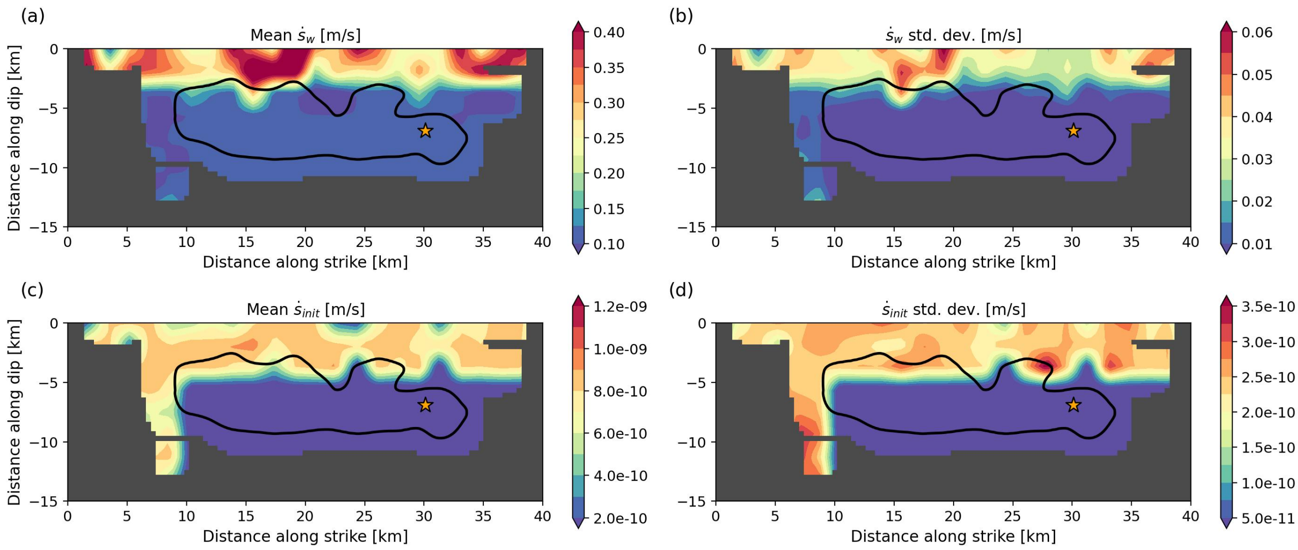

Figure S14. Mean distributions of the best-fitting model ensemble's (a) weakening slip rate $\dot{s}_w0$, (c) initial slip rate $\dot{s}_{init}$, and the corresponding standard deviations (b,d). The model ensemble contains 10500 models. We hide areas where the sum of coseismic and postseismic slip does not exceed 10 cm within 1.2 km, which we consider unconstrained.

Table S1. 1D velocity profiles on the southwest and northeast side of the fault (Custódio et al., 2005) used to calculate the Green's functions. The dynamic rupture solver uses the average velocity profile. Q values are based on v_s: $Q_s = 0.1\,v_s$ (in m/s) and $Q_p = 1.5\,Q_s$ (Olsen et al., 2003).

Lower extent [km]	v_p [m/s]	v_s [m/s]	Density [kg/m^3]	Q_p	Q_s
		southwest			
1.0	2000	1100	2000	165	110
2.0	3500	2000	2300	300	200
3.0	4500	2500	2300	375	250
3.5	5200	3000	2500	450	300
5.8	5700	3200	2700	480	320
14.1	6200	3600	2700	540	360
17.1	6800	3600	2800	540	360
20.4	6800	4300	2800	645	430
∞	7300	4300	2800	645	430
		northeast			
1.0	2000	1100	2000	165	110
1.8	3500	2200	2300	330	220
2.1	4200	2800	2300	420	280
3.4	4800	2700	2300	405	270
3.9	5200	2800	2300	420	280
8.3	5300	3200	2700	480	320
12.7	5700	3700	2800	555	370
17.5	6500	3800	2800	570	380
20.3	6700	4300	2800	645	430
∞	7300	4300	2800	645	430
		average			
1.0	2000	1100	2000	165	110
2.0	3500	2100	2300	315	210
3.5	4400	2700	2300	405	270
5.8	5500	3000	2500	450	300
12.7	5800	3600	2700	540	360
17.1	6500	3800	2800	570	380
20.3	6800	4300	2800	645	430
∞	7300	4300	2800	645	430

Table S2. Step size ranges of the model parameter perturbations during the inversion. The parameter perturbations are drawn from a log-normal distribution and the step size represents its relative standard deviation. The step size is successively reduced to keep the model acceptance rate reasonable.

Label	Parameters	Log-normal step size (in %)
τ_0	Shear prestress	0.3–2.0
b	state evolution parameter	0.3–2.0
f_0	Reference friction coefficient at $\dot{s}_0 = 10^{-6}$	0.3–2.0
L	Characteristic slip distance	0.3–2.0
$\dot{s}_w$	Weakening slip rate	0.3–2.0
$\dot{s}_{init}$	Initial slip rate	2.0
h_x	Along-strike position of nucleation patch	0.3–2.0
h_z	Along-dip position of nucleation patch	0.3–2.0
r_{nuc}	Radius of the nucleation patch	0.3–2.0
σ_{nuc}	Stress increase within the nucleation patch	0.3–2.0

References

Custódio, S., Liu, P., & Archuleta, R. J. (2005). The 2004 Mw6.0 Parkfield, California, earthquake: Inversion of near-source ground motion using multiple data sets. *Geophysical Research Letters*, *32*.

Jiang, J., Bock, Y., & Klein, E. (2021). Coevolving early afterslip and aftershock signatures of a San Andreas fault rupture. *Science Advances*, *7*.

Ma, S., Custódio, S., Archuleta, R. J., & Liu, P. (2008). Dynamic modeling of the 2004 Mw 6.0 Parkfield, California, earthquake. *Journal of Geophysical Research: Solid Earth*, *113*.

Neves, M., Peng, Z., & Lin, G. (2022). A High-Resolution Earthquake Catalog for the 2004 Mw 6 Parkfield Earthquake Sequence Using a Matched Filter Technique. *Seismological Research Letters*, *94*.

Olsen, K. B., Day, S. M., & Bradley, C. R. (2003). Estimation of Q for Long-Period (>2 sec) Waves in the Los Angeles Basin. *Bulletin of the Seismological Society of America*, *93*.